Remote Sensing of Environment 314 (2024) 114389

Contents lists available at ScienceDirect

Remote Sensing of Environment

journal homepage: www.elsevier.com/locate/rse

Assessment of the spaceborne EnMAP hyperspectral data for alteration mineral mapping: A case study of the Reko Diq porphyry Cu—Au deposit, Pakistan

Saeid Asadzadeh [a,*], Xiaodong Zhou [b], Sabine Chabrillat [a,c]

[a] Section of Remote Sensing and Geoinformatics, Helmholtz Centre Potsdam, GFZ German Research Centre for Geosciences, 14473 Potsdam, Germany
[b] Independent Spectral Geology and Remote Sensing Consultant, Toronto, Canada
[c] Leibniz University Hannover, Institute of Soil Science, 30419 Hannover, Germany

ARTICLE INFO

Edited by: Jing M. Chen

Keywords:
EnMAP satellite
Imaging spectroscopy
Mineral chemistry
Vector minerals
Polynomial fitting
Porphyry exploration
Chagai province

ABSTRACT

For over four decades, spaceborne multispectral data have played a crucial role in supporting mineral exploration and geologic mapping. The spaceborne multispectral datasets, however, have a restricted number of bands with coarse spectral resolution and, thus are very limited in mineral mapping. The advent of high-quality spaceborne imaging spectroscopic data like the Environmental Mapping and Analysis Program (EnMAP), has bridged this gap initiating a new era in global hyperspectral mineral mapping. The EnMAP satellite, operational since November 2022, covers the spectral range of 420 and 2450 nm in 224 bands, offering a spatial resolution of 30 m and a mean spectral sampling distance of 8.1 and 12.5 nm in the visible-near infrared and shortwave infrared regions, respectively. In this paper, we demonstrate the enhanced mapping capabilities of EnMAP using datasets acquired over the Reko Diq mining district, a cluster of Miocene porphyries located in Pakistan's Chagai Belt hosting an undeveloped world-class porphyry Cu-Au ± Mo deposit. The EnMAP's Level 2A data product was processed using the polynomial fitting technique to characterize the diagnostic absorption features of the alteration minerals in the Reko Diq porphyry system. This involved retrieving the minimum wavelength, depth, width, and asymmetry parameters for key absorption features and employing them interactively for mineral characterization. A diverse array of minerals were successfully mapped over the study area and validated by ground spectroscopy. This includes abundance/composition maps for white micas, chlorite, epidote, calcite, kaolinite, gypsum, jarosite, and ferric and ferrous iron minerals. The minimum wavelength of white mica was found to vary between 2195 and 2210 nm, with the shorter wavelengths (Al-rich) white mica occurring proximal to the known mineralized zones. The potassic alteration cores and the outer propylitic zones were identified by the ferrous iron and chlorite-epidote-calcite mineral maps, respectively. This study demonstrated the superiority of EnMAP hyperspectral data in delineating the alteration mineralogy and zonation pattern of porphyry copper systems. This capability can potentially contribute to the exploration of new deposits in exposed terrains worldwide.

1. Introduction

Multispectral satellite imagery, such as Landsat and Advanced Spaceborne Thermal Emission and Reflection Radiometer (ASTER) data, has been extensively used over the past decades to assist mineral exploration and geologic mapping worldwide. The critically configured spectral bands, coupled with moderate spatial resolution, global coverage, and free accessibility have made these datasets a cost-effective and widely used tool for regional mapping of hydrothermal alteration minerals, discriminating between different rock types, and generating exploration targets for follow-up field mapping and sampling (Di Tommaso and Rubinstein, 2007; Goetz et al., 1983; Mars and Rowan, 2006; Pour and Hashim, 2012; Rowan et al., 2006; Sabins, 1999; van der Meer et al., 2012; Zhou et al., 2017). These multispectral datasets, however, have a limited number of bands with a relatively broad spectral resolution in the visible-near infrared (VNIR) and shortwave infrared (SWIR) regions, resulting in uncertainties in mineral identification and mapping. Consequently, discrimination is restricted to mineral groups only,

* Corresponding author.
E-mail addresses: saeid@gfz-potsdam.de (S. Asadzadeh), Sabine.chabrillat@gfz-potsdam.de (S. Chabrillat).

https://doi.org/10.1016/j.rse.2024.114389
Received 19 March 2024; Received in revised form 20 August 2024; Accepted 24 August 2024
Available online 30 August 2024

and the level of confidence given to the mapped minerals is not always high, with the outcomes often failing to accurately depict the full spatial extent of particulate minerals or differentiating between spectrally similar minerals co-occurring in a pixel (Dalton et al., 2004; van der Meer et al., 2012). Furthermore, multispectral datasets fall short in consistently detecting the variations observed in mineral chemistry, thereby impeding effective vectoring within the lithocap towards mineralized centers.

The high-resolution multispectral data have enabled improved mineral mapping capabilities. For instance, Worldview-3 multispectral data at 3.7 m spatial resolution in the SWIR region allows mapping for smaller and/or weaker alteration zones, as well as more accurate mineral identification for phyllosilicates at deposit to district scales (Coulter et al., 2017). Worldview-3 together with Sentinel-2 satellite data also enables improved mapping for ferric and ferrous iron minerals, including jarosite, goethite, and hematite discriminations (Mars, 2018; Van der Werff and Van der Meer, 2015). Despite these improvements, however, the fundamental limitations described above still apply to these datasets.

In contrast, hyperspectral imaging (also referred to as imaging spectroscopy) at medium to high spatial resolution is a proven technology for the systematic mapping of alteration minerals associated with various hydrothermal mineral systems. Four decades of airborne hyperspectral data have proved the technology and its wide applicability in the field of geology and mineral exploration (Bedini, 2017; Berger et al., 2003; Clark et al., 2003; Cudahy et al., 2008a; Cudahy et al., 2001; Kruse et al., 2003). The finer spectral resolution of hyperspectral datasets allows them to capture more detailed information about the spectral signatures of minerals, resulting in more accurate mineral mapping and improved discrimination capabilities compared to multispectral data (van der Meer et al., 2012). This technology has played a key role in advancing our understanding of alteration zonation, identifying the large-scale footprint of mineral systems, and mapping the chemistry of vector minerals (comprising the Tschermak substitution[1] in white mica (Duke, 1994)), facilitating ore targeting and exploration drilling (Asadzadeh et al., 2023; Cudahy, 2016; Graham et al., 2018; Portela et al., 2021; Swayze et al., 2014; Uribe-Mogollon and Maher, 2020).

The airborne surveys, however, are restricted to specific regions and lack global coverage due to cost and logistic hurdles. Since the inception of the Hyperion/EO-1 demonstration mission in 2000, the potential of high-quality spaceborne hyperspectral data has been recognized, leading to numerous efforts to launch imaging spectroscopy systems into orbit. Today, a range of spaceborne hyperspectral missions, comprising DLR Earth Sensing Imaging Spectrometer (DESIS), PRecursore IperSpettrale della Missione Applicativa (PRISMA), Hyperspectral Imager Suite (HISUI), Advanced Hyperspectral Imager aboard China's Gaofen-5 satellite, Earth Surface Mineral Dust Source Investigation (EMIT), and Environmental Mapping and Analysis Program (EnMAP) offer medium spatial resolutions data from the Earth's surface (Alonso et al., 2019; Cogliati et al., 2021; Green, 2022; Guanter et al., 2015; Liu et al., 2019; Matsunaga et al., 2022). While the potential of spaceborne hyperspectral imaging data for mineral exploration purposes is promising (e.g., Chirico et al., 2023; Dong et al., 2022), the effectiveness and utility of EnMAP data for raw material exploration are yet to be substantiated using real operational datasets.

This study aims to assess the applications of EnMAP hyperspectral data in the field of geology and mineral exploration by studying the world-class Reko Diq porphyry Cu-Au-Mo deposit in the Chagai Belt, Baluchistan province of Pakistan. It also seeks to test the effectiveness of spectroscopic-stemmed processing techniques and algorithms in the analysis of EnMAP hyperspectral data for accurate mineral characterization and mapping. Reko Diq has been the focus of several remote sensing studies over the past decades, including a study using the Landsat-1 data (Schmidt, 1976) and a subsequent analysis using the ASTER instrument (Rowan et al., 2006). The bedrock geology and the alteration patterns of this deposit are well-documented by surface and subsurface mapping, ground spectroscopy, and geochemical analysis. The existence of previous remote sensing studies from the ASTER instrument, the well-exposed bedrock, and the sheer size of the Reko Diq deposit—recognized as one of the largest undeveloped porphyry copper deposits in the world with minimum surface disturbances—makes this site an ideal choice for remote sensing mapping. It also provides a solid basis for evaluating the enhanced capability of the EnMAP instrument in alteration mineral mapping.

Porphyry copper deposits typically exhibit large and concentric zoned alteration, with potassic alteration of biotite-orthoclase at the core, upwards and outwards to phyllic alteration of quartz-sericite-chlorite and then propylitic alteration of epidote-chlorite-carbonates, overprinted (and overlaid) by intermediate argillic alteration of illite-kaolinite-montmorillonite and/or advanced argillic alteration of quartz-alunite-pyrophyllite-kaolinite-dickite (Seedorff et al., 2005; Sillitoe, 2010). This generalized model reflects the evolution of hydrothermal fluids from near-neutral, high-temperature conditions to cooler more acidic fluids over space and time.

Given the recent classification of copper as a critical raw material (Energy, U.S.D.o, 2023), there is an immediate need to enhance exploration programs to meet the rising demand for copper resources during green transitions. Porphyry copper deposits, which account for nearly 70 % of global copper production (Singer, 2017), continue to be a valuable target for spectral remote sensing studies.

2. Geology of the Reko Diq deposit

The world-class Reko Diq copper-gold ± molybdenum porphyry deposit is located in the east-west trending Chagai magmatic belt of northwest Balochistan Province, Pakistan (Fig. 1). The region is characterized by mountain ranges of low-moderate relief interspersed by sandy and stony pediplains over topographic depressions, with extremely arid conditions, sparse vegetation cover, and generally shallow chemical weathering. At Rekndo Diq, the bedrocks are partially covered by alluvial-fluvial deposits, and locally by a veneer of Fe-stained eolian quartz sands (Perelló et al., 2008; Rowan et al., 2006).

The Reko Diq igneous complex contains a cluster of 18 individual porphyry centers, within a 10 km × 3 km NW trending mineralized corridor which is bounded by the Drana-Koh fault system to the north and the Tuzgi fault to the south. It is estimated to contain a global resource of 5900 million metric tons @ 0.41 % Cu and 0.22 g/t Au (Perelló et al., 2008; Razique et al., 2014), with the majority of reserves located in the western porphyry systems (i.e., H79, H15, H14, and H13), the Tanjeel system, and the H8 and H35 sub-systems (Fig. 1). Porphyry Cu—Au mineralization at Reko Diq is spatially and temporally associated with the Miocene calc-alkaline granodiorite and quartz-diorite to diorite porphyry stocks and dykes (Fig. 1) emplaced into the Early Miocene felsic-intermediate-mafic volcanic and subvolcanic country rocks of the Reko Diq Formation and the underlying Late Oligocene clastic sedimentary rocks of the Dalbandin Formation in a continental arc setting (Razique et al., 2014; Zürcher et al., 2019).

Although each of the porphyry systems in the cluster originates from spatially separate and temporally distinct porphyry intrusives, the resulting hydrothermal alteration and mineralization exhibit significant spatial overlap (Razique et al., 2014). The alteration halos of H14-H15 porphyry centers, for instance, are coalesced and zoned from potassic (biotite+K-feldspar) outboard to phyllic (quartz-sericite+/−chlorite) and distal propylitic (chlorite-epidote+/−carbonate) alteration. Potassic alteration is overprinted by phyllic alteration which in turn is overprinted by intermediate argillic alteration. Advanced argillic alteration is uncommon in the study area (Razique et al., 2014).

High-grade mineralization of disseminated and veinlet

[1] The substitution of elements within a mineral crystal structure.

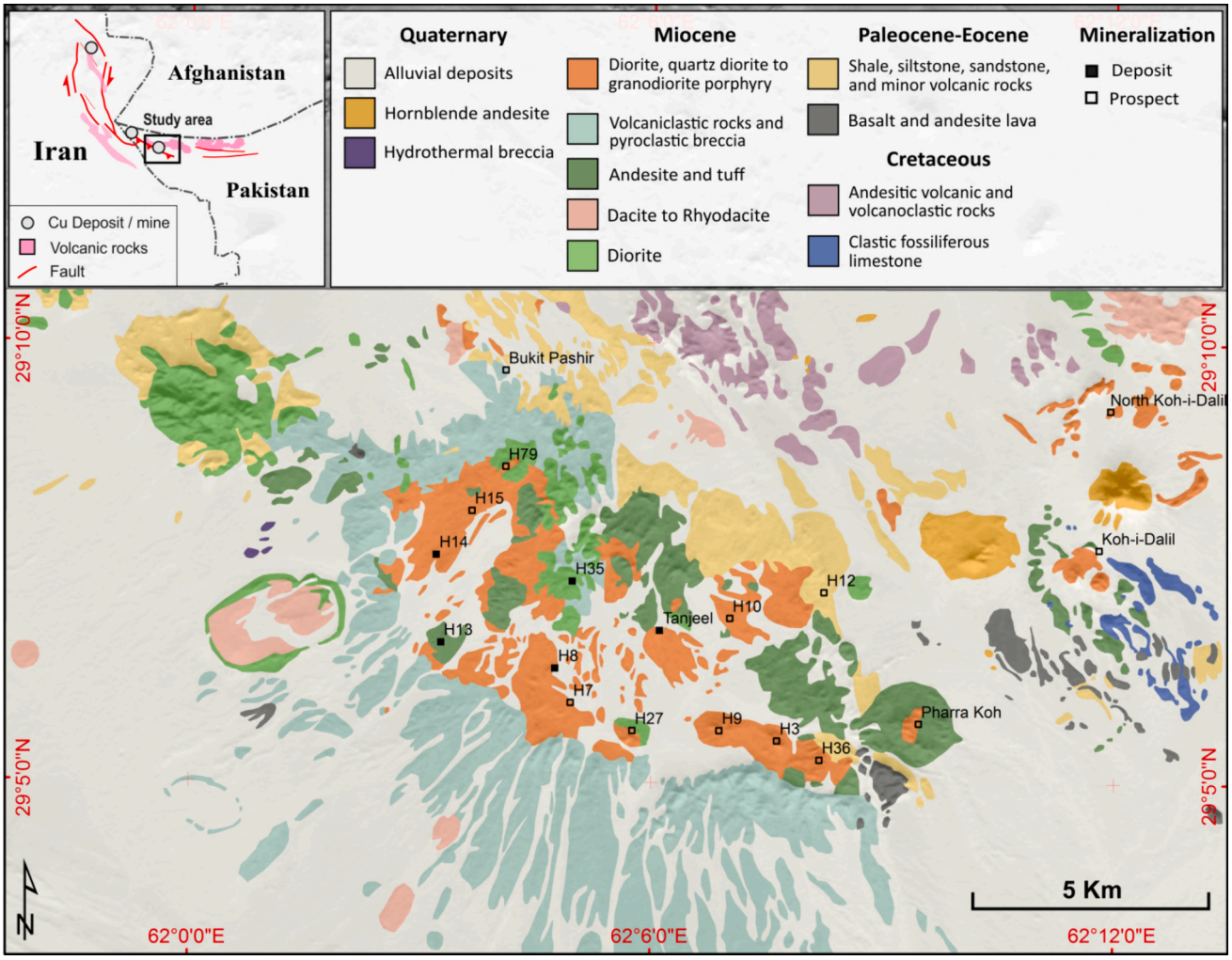

Fig. 1. Simplified geologic map of the area adopted from Razique et al. (2014) and modified/improved through visual image interpretation techniques using orthorectified satellite data. The deposit/prospect locations and naming were extracted from Ürcher et al. (2015).

chalcopyrite+/−bornite is associated with intensive potassic alteration and A-type veins in early mineral granodiorite and intro-mineral quartz-diorite intrusions and adjacent country rock. Of all mineralized porphyry centers in the district, significant supergene enrichment is found only at the Tanjeel porphyry system where a relatively large supergene chalcocite blanket occurs beneath a 40-50 m thick leached cap of supergene kaolinite+/−alunite, residual hydrothermal quartz and sericite, quartz-limonite veins, Fe oxides (jarosite+hematite+/−geothite) and Cu oxides (chalconthite+/−chrysocolla) (Perelló et al., 2008).

3. The EnMAP satellite data

The Environmental Mapping and Analysis Program (EnMAP) satellite was successfully launched into orbit on April 1, 2022, by a Falcon 9 rocket from Cape Canaveral in Florida. The commissioning phase completed by the end of October 2022, marked the successful initiation of its operational phase (Storch et al., 2023). Since then, the instrument has been routinely collecting data worldwide. EnMAP is a German hyperspectral satellite system designed to provide high-quality, well-calibrated data for environmental monitoring and sustainable management of the Earth's natural resources (Chabrillat et al., 2022). Specifications of the sensor and satellite system are summarized in Table 1. Additional information about the instrument, data processing levels, and data access can be found in Guanter et al. (2015) and Storch et al. (2023) as well as the EnMAP portal at www.enmap.org.

Table 1
The specification of the EnMAP satellite system (source: www.enmap.org).

Spectral range	VNIR	SWIR
	420–1000 nm	900–2450 nm
Spectral sampling interval	6.5 nm	10 nm
Spectral bandwidth (FWHM)	8.1 nm	12.5 nm
Number of spectral bands	95	135
Signal-to-noise-ratio (SNR)	>470:1	>250:1
Spectral stability	0.5 nm	1 nm
Radiometric resolution	14 bits	
Geolocation accuracy	<30 m	
Co-registration accuracy	0.3–0.4 pixel	
Geometric resolution	30 m × 30 m	
Swath	30 km	
Revisit time	27 days @ ±5° off-nadir tilt 4 days @ ±30° off-nadir tilt	
Operational lifetime	> 5 years	
Equator crossing time	11:00 h ± 18 min.	

4. Materials and methods

The datasets used herein include EnMAP data covering the deposit and surrounding areas, detailed geology (and alteration) maps (as depicted in Fig. 1), and field spectroscopy conducted over deposit outcrops.

4.1. EnMAP data acquisition and preprocessing

The EnMAP data over the target area was obtained upon our request on November 8th, 2022 at 07:10:35 UTC (12:10 local time). At the time of acquisition, the solar zenith angle was 46.13°. The Level 2A EnMAP orthorectified surface reflectance product comprising 224 consecutive spectral bands at 30-m resolution in BSQ format was ordered from the EOWEB® Geoportal. The data were processed by the ground segment with the following setting: 'L2A processing with atmospheric correction for land surfaces' with ozone correction activated, with no terrain correction and spectral interpolation, and resampling using the nearest neighbor method. A subset of the original EnMAP 30 × 30 km tile covering an area of 500 km^2 was prepared for processing in this study. Although a new EnMAP processor was introduced at the end of March 2023, which largely eliminates the striping noise of the sensor, we primarily employed the datasets provided by the old processor for this study. Accordingly and as the first step, the striping noise was removed in the frequency domain using the Fast Fourier Transform (FFT) technique (Asadzadeh et al., 2019). In this approach, all the bands, except the atmospheric bands, were transformed into the frequency, and their systematic noise was isolated and removed. The image was then transformed back into the image/spectral domain, resulting in a de-noised dataset suitable for spectral mineral mapping.

4.2. Spectral mineral mapping

We refined the fitting to the minimum technique described by Rodger et al. (2012) by allowing it to search for the minimum within a user-specified wavelength range. For this aim, the local continuum is first removed over the desired absorption feature(s), by fitting a straight line to the side shoulders (Clark et al., 2003). Then the wavelength of minimum reflectance (also known as minimum wavelength) is determined by fitting a quadratic or a higher-order polynomial to the apparent minimum and its adjacent bands located within the user-specified range. For the quadratic fitted polynomial, the root of the explicit first derivative is used to accurately determine the minimum wavelength of the absorption feature (Rodger et al., 2012). In the case of higher-order polynomials, the (real) roots of the explicit first derivative are derived from the Lagrange method (Asadzadeh and Souza Filho, 2016). The depth of the feature is subsequently retrieved from the coefficients of the fitted polynomial relative to the continuum hull. The method also retrieves the width, area, and asymmetry of the absorption feature following the procedures described in Asadzadeh and Souza Filho (2016). When the retrieved wavelength falls within the user-defined range, the second derivative of the fitted polynomial is positive, and the absorption depth exceeds a user-defined threshold, then the feature is considered a true absorption feature, and the extracted spectral parameters are stored for further analysis. The feature width is calculated at a depth level set by the user, ranging from 50 % (equivalent to FWHM; full-width-half maximum) to 90 % of the absolute depth. The obtained spectral parameters are subsequently stored and used for both identifying and characterizing the target minerals, including mapping the occurrences, relative abundances, and any compositional variations. This methodology also enables the detection of mineral mixtures in the data. Here, it is assumed that the continuum-removed absorption depth is proportional to the relative abundance of the corresponding mineral and the minimum wavelength is proportional to the cation composition of the mineral revealing its physicochemistry (Cudahy et al., 2008a).

In our processing chain, multiple features are incorporated into the decision-making process to enhance the accuracy of mineral identification and mapping. However, instead of evaluating and thresholding the spectral parameters individually, we employ a pair of spectral parameters presented in a scatterplot to interactively isolate a specific mineral/feature within the image data. For instance, the Al–OH absorption depth at 2200 nm plotted against the kaolinite absorption depth at ~2165 nm is used to distinguish kaolinite-dominated pixels from white mica. Moreover, by examining the scatterplots of the retrieved spectral parameters (e.g., the minimum wavelength against depth) further insights about the state of the minerals including the spectral mixtures between minerals are obtained. To track the relative variations in the proportion of absorption features, two absorption depth ratios comprising Mg–OH/Al–OH and Fe–OH/Mg–OH were introduced and tested (detailed below). Additionally, a new spectral index was developed to differentiate between low-temperature illite and high-temperature sericitic (muscovite) white mica, as detailed below.

Based on our general understanding of alteration mineralogy in porphyry copper deposits and previous studies conducted in the Reko Diq area outlined above, a set of spectrally active (and spatially mappable) minerals were nominated for remote sensing mapping using the EnMAP hyperspectral data. These minerals along with the processing methodology used for their identification and quantification are summarized in Table 2.

White mica was identified based on the presence of a prominent Al–OH absorption at 2200 nm, the existence of an additional absorption at ~2350 nm, and the absence of a kaolinite absorption at ~2165 nm (Cudahy et al., 2008b). To achieve this, a 2nd-order polynomial was fitted to the wavelength range between 2180 and 2225 nm after removing the continuum between 2120 and 2250 nm. The resulting depth and wavelength values were then utilized to represent the abundance (2200D) and chemical composition (Tschermak substitution level (Duke, 1994); 2200W) of the white mica, respectively.

The secondary absorption feature of kaolinite at 2165 nm was characterized by fitting a 2nd-order polynomial to the range of 2155–2182 nm (continuum removed between 2120 and 2250 nm range). The plot of 2200D against 2165D was then used to identify this mineral within the EnMAP data. In this plot, kaolinite-bearing pixels are linearly distributed and show a significant positive correlation (see below). The absorption depth at 2165 nm (2165D) was used to represent the relative abundance of kaolinite. Due to the scarcity of kaolinite in the area, the crystallinity index was not calculated for this mineral.

In an attempt to distinguish between white mica of muscovite (sericite) and illite composition, two distinct differences were recognized between these minerals: (i) muscovite retains an additional absorption feature at 2120 nm, which is mostly absent in illite (see, for example, Fig. 2a) (ii) illite's Al–OH feature at 2200 nm is wider and more asymmetric rightward compared to muscovite. By considering the first distinction, the ratio of R_{2080}/R_{2118} (where R_λ represents reflectance at wavelength λ) was used to highlight the pixels dominated by high-temperature muscovite in the study area.

To characterize the double absorption features of chlorite centered at 2250 nm (Fe–OH) and 2340 nm (Mg–OH), 4th-order polynomials were fitted to the interval between 2224 and 2282 nm and 2282–2377 nm, respectively (see Table 2). Given that chlorite and epidote exhibit similar absorption features in this range, what is yielded by this method is a mixture of both minerals. To differentiate between them, additional spectral products were developed and tested: (i) the diagnostic absorption feature at 1550 nm to identify epidote-bearing pixels. For this aim, the ratio of R_{1587}/R_{1542} was calculated and the (filtered) result plotted against 2340D was used to isolate epidote-dominated pixels (Table 2). The outcomes, masked for topographic shadows, represent the epidote's abundance (1550D). (ii) The ratio between Fe–OH and Mg–OH depth (2250D/2340D; Table 2) to separate epidote from chlorite. Theoretically, chlorite and epidote should exhibit ratio values >0.6 and < 0.6, averaged around 0.8 and 0.5, respectively (see Supplementary Fig. S1a). (iii) The absolute difference between Mg–OH and Fe–OH depth (2340D – 2250D). Chlorite is expected to exhibit index values between 0.03 and 0.12 (on average, 0.07), while epidote tends to have values >0.25 (on average, 0.28). (iv) The absolute difference in the minimum wavelength of the Fe–OH and Mg–OH features (2340 W – 2250 W). This index should yield a relatively constant value for epidote (i.e., 82 nm), while for chlorite, it ranges between 75 and 92 nm for Mg-rich and Mg-poor species, respectively. The other product, developed to highlight the

Table 2
Spectral mineral products derived from the analysis of EnMAP hyperspectral data over the Reko Diq porphyry copper deposit. The table contains a summary of the distinctive absorption features and the scripts used for mineral detection and characterization. The scripts are adopted and modified after (Cudahy et al., 2008a; Laukamp et al., 2021; Roache et al., 2011). λD is the depth of an absorption feature at wavelength λ, and λW represents the minimum wavelength of that same feature. Note that the wavelength range used for continuum removal (CR) differs from the range used for polynomial fitting.

Mineral	Distinctive features	Product ID	CR range (nm)	Mapping script	Mapping result
White mica	Al–OH bands at 2200 and 2350 nm	2200D 2200W	2120–2250	A fitted 2nd-order polynomial to the apparent minimum between 2180 and 2225 nm constrained by the lack of a kaolinite feature at ~2165 nm and the existence of an additional absorption feature at ~2350 nm.	Figs. 3c-d
Kaolinite	Asymmetrical Al–OH doublets at 2165 and 2205 nm	**2165D**	2120–2250	A fitted 2nd-order polynomial to the apparent minimum between 2155 and 2182 nm. The scatterplot of 2200D versus 2165D was used interactively to identify kaolinite.	Fig. 4a
Chlorite (±epidote)	Mg–OH features between 2310 and 2370 nm. A Fe–OH absorption feature near 2250 nm	**2250D** **2250W** **2340D** **2340W**	2174–2392	**Fe–OH:** A fitted 4th-order polynomial between 2224 and 2282 nm. **Mg–OH:** A fitted 4th-order polynomial between 2282 and 2377 nm.	Figs. 4c-d Figs. 4e-f
Epidote	Two Fe–OH features at ~2258 and 2340 nm. A subordinate OH feature near 1550 nm	**1550D**	–	The ratio of R_{1587}/R_{1542} , smoothed by a median filter (1550D), plotted against 2340D (see Fig. 8d) to isolate the epidote-bearing pixels.	Fig. 5a
Gypsum	Multiple H_2O, OH, and S—O features at 1540, 1750, and 2210 nm.	**1750D**	–	The ratio of R_{1685}/R_{1759} (1750D) plotted against 2200D to isolate the gypsum-bearing pixels.	Fig. 7b
Jarosite	Broad 900 nm feature Distinctive Fe–OH and S—O feature between 2240 and 2290 nm	**2265D**	2135–2345	The continuum-removed depth at 2266 nm plotted against 2200D to isolate jarosite-bearing pixels. This was constrained by 900D > 0.087 and masked for topographic shadow.	Fig. 7a
Ferrous Iron	Broad electronic transition absorptions between 1000 and 1300 nm	**1100D**	–	Ferrous iron abundance derived by applying $(R_{920}+R_{1650})/(R_{1030}+R_{1230})$, stretched between 1.07 and 1.143.	Fig. 5d
Ferric iron	Broad charge transfer feature at ~900 nm	**900D** **900W**	770–1080	A fitted 2nd-order polynomial between 770 and 1080 nm following spectral smoothing using the Boxcar filter (width = 7). The plot of 900 W against 900D was used to highlight ferric iron pixels.	**Figs. 7 c-d**

overprinting effects of chlorite on white mica, was obtained by dividing the feature depth at 2350 nm (shared between white mica and chlorite) to 2200D. This ratio map was masked by the white mica occurrence and smoothed using a median filter. No independent product was developed for calcite, and the identification of calcite-bearing pixels was based on the 2250D/2340D index and the fact that calcite lacks a feature at 2250 nm and a ferrous iron feature in the VNIR.

To evaluate the effectiveness of the indices developed here for distinguishing chlorite from epidote, we utilized the spectral library of calcite-epidote-chlorite synthetic mixtures as described in Dalton et al. (2004). We employed a similarity metric based on the coefficient of determination (R^2) aiming to compare them against the continuum-removed image spectra, analogous to the methodology implemented in the Tetracorder package (Dalton et al., 2004). However, instead of generating a classification map, we retrieved the proportion of each mineral in the matched spectra to create relative abundance maps. The results were then combined to represent calcite, epidote, and chlorite as RGB components.

The spatial occurrences of gypsum and jarosite were mapped using the scripts provided in Table 2. In the case of gypsum, the plot of 1750D (estimated by R_{1685}/R_{1759} ratio) against 2200D was used to identify gypsum-bearing pixels. The assumption here is that the presence of white mica has obscured the 2210 nm feature of gypsum (and anhydrite) (Asadzadeh et al., 2023). However, given the co-occurrences of gypsum with white mica in porphyry copper deposits, the noted scatterplot should effectively accentuate the subtle occurrences of gypsum in the area. The continuum-removed depth at 2266 nm (continuum removed between 2135 and 2345 nm range) plotted against 2200D was used to detect jarosite. The results were constrained by 900D > 0.087 (see Table 2) and further masked out by topographic shadow. The depth at 2266 nm represents the relative abundance of jarosite. The shadow mask was derived by thresholding the EnMAP band at 1675 nm ($R_{1675}<0.215$ in re-scaled data).

To detect the broad Fe^{2+} absorption feature associated with electronic transitions, a simple band ratio (i.e., $(R_{920}+R_{1650})/(R_{1030}+R_{1230})$ adapted from Cudahy et al. (2008a)) was applied to reflectance data. With the new EnMAP processor, the mismatch between VNIR and SWIR bands has been significantly reduced. Accordingly, we utilized the new processor product to map ferric iron minerals. For this aim, a 2nd-order polynomial was fitted within the wavelength range of 770 to 1080 nm, following spectral smoothing using a Boxcar filter (width = 7; Table 1). The plot of 900 W against 900D was utilized to isolate pixels with ferric iron minerals, and the outcome was masked for topographic shadow.

All the resulting mineral maps were color-coded and overlaid onto an albedo image to better represent the variations in the desired spectral parameters. To improve the representations, linear stretching was applied to all grayscale data. For the 2200D, 2250D, 2340D, and 1100D maps, however, a logarithmic conversion (log(depth × 100)) was employed beforehand to show the variations more clearly.

To enable a comparison between the spectroscopic-based technique and standard machine learning methods, we employed the Support Vector Machine (SVM) classification algorithm. Eight training classes were manually defined over the EnMAP data and the entire cube was processed using a 3rd-degree polynomial kernel type. The classes include sericite and propylitic alteration, kaolinite, sand dunes, and three classes representing the country rocks (not depicted in the final map). In addition to mineral maps, specific scatterplots were also created to elucidate the methodology and highlight the prevalent mineral mixtures in the study area. In the end, selected spectral plots derived from single pixels were compared to the USGS spectral library (Kokaly et al., 2017) to visualize the mineral mixtures and assess the reliability and validity of the EnMAP hyperspectral data as well as the processing methods.

4.3. Ground spectroscopy

As part of the Reko Diq mapping and drilling program conducted by Barrick Gold in the mid-2000s, spectral measurement was conducted using an ASD Terraspec Pro spectrometer along multiple transects crossing the porphyry centers. The Terraspec Pro instrument collects data within the wavelength range of 350 to 2500 nm at 3–6 nm spectral resolution. A Spectralon panel was used to convert the measurements into reflectance. These measurements were obtained from outcrops on

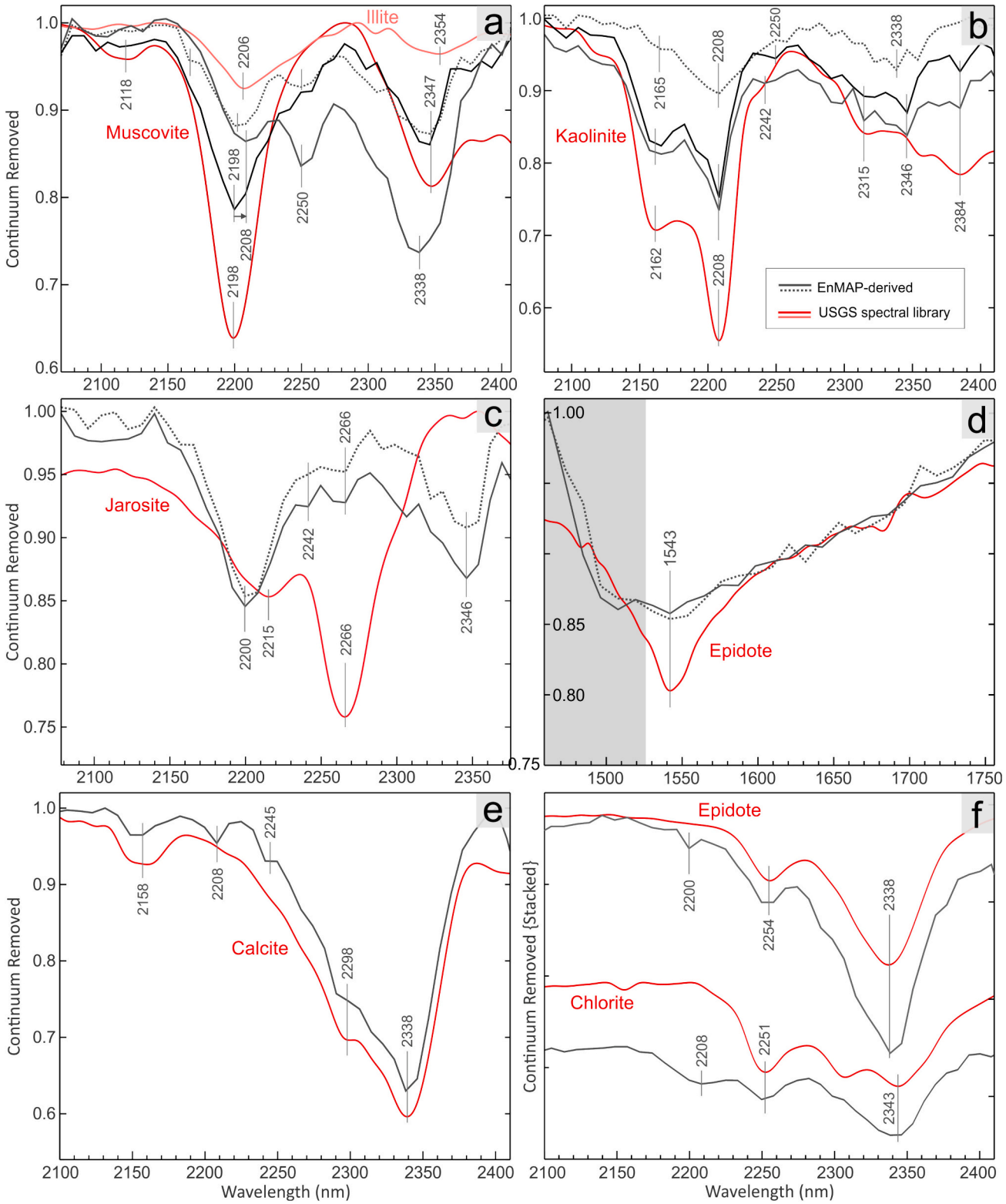

Fig. 2. The EnMAP-derived spectra (solid and dashed gray lines) compared with the USGS spectral library (solid red line) published by Kokaly et al. (2017): **a)** various compositions of white mica mixed with chlorite and trace amounts of kaolinite. The muscovitic white mica displays an extra absorption feature at 2118 nm, which is typically absent in illite, **b)** kaolinite with trace amounts of white mica and chlorite, **c)** jarosite mixed with white mica with trace amounts of chlorite, **d)** epidote at around 1550 nm wavelength range. The gray shade marks the added bands in the new EnMAP processor, **e)** calcite with traces of clays and chlorite, **f)** epidote and chlorite with trace amounts of white mica. Note that the presented spectral data has not undergone any smoothing/polishing. (For interpretation of the references to color in this figure legend, the reader is referred to the web version of this article.)

the ground using a contact probe under artificial illumination. A subset of this collection was used here to validate the results of spectral analysis and assess the effectiveness of EnMAP data in mapping surface mineralogy.

5. Results

5.1. Visual inspection of EnMAP's spectral content

Visual inspection of the spectral plots from image pixels reveals a significant level of concordance between the EnMAP-derived spectra and the USGS spectral library (Fig. 2). However, most pixel spectra show a complex mixture of two to three minerals, supporting the interpretations made in the image and feature domains (see below). This includes white mica (with characteristic features at 2200 and 2350 nm) mixed with chlorite (features at 2250 and 2338 nm) and kaolinite (subtle feature at 2165 nm; Fig. 2a). Pixels from the phyllic zone show a noticeable shift of up to 10 nm in the minimum wavelength of white mica (Fig. 2a), with some displaying a feature at 2118 nm characteristic of muscovite-dominated pixels. Fig. 2b illustrates varying proportions of kaolinite in image pixels, mainly mixed with white mica (feature at 2346 nm) and chlorite (2242–50 and 2338 nm). Note that EnMAP has successfully resolved the subtle feature of kaolinite at 2384 nm.

Fig. 2c draws a comparison between the spectrum of jarosite and a jarosite-bearing pixel spectrum. In most pixels, jarosite (with a diagnostic feature at 2266 nm) is found to be intimately mixed with white mica (with features at 2200 and 2346 nm) and occasionally with chlorite (with features at 2242 nm). Based on Fig. 2d, the EnMAP data can resolve the subtle feature of epidote at 1550 nm, although its left shoulder appears to be overestimated compared to the USGS spectral library. This discrepancy could potentially explain why the polynomial fitting technique was not effective in resolving this feature (see below). Fig. 2e compares the spectral plot of calcite indicated by a diagnostic absorption feature at 2338 nm. The image pixel, though, shows traces of clay co-occurrences marked by features at 2208 and 2245 nm. The extracted spectra for epidote (with features at 2254 and 2338 nm) and chlorite (with features at 2251 and 2343 nm) compare well with the reference data (.Fig. 2f), demonstrating the high quality of EnMAP in the far end of the SWIR range enough to discriminate the faint absorption features of typically dark Mg–OH minerals. Note that the chlorites observed in the phyllic zone depicted in Figs. 2a-b are Mg-rich in composition.

5.2. Spectral mineral mapping

Figs. 3–7 present the EnMAP true- and false-color imagery (Figs. 3a-3b), along with the mineral maps acquired over the study area, including white mica composition and abundance (Figs. 3c-3f), kaolinite occurrence and abundance (Figs. 4a-4b), chlorite, epidote, and calcite abundance and composition (Figs. 4c-4f and 5a-5c), ferrous iron minerals (Fig. 5d), spectral similarity mapping (Fig. 6a), SVM-derived classification map of major alteration assemblages (Fig. 6b), secondary sulfate minerals (Figs. 7a-7b), and maps of ferric iron minerals (Figs. 7c-7d). The locations of ground spectroscopic measurements are depicted in Fig. 3a.

In the true color composite image (Fig. 3a), the hydrolytic (hydrogen-ion metasomatism comprising phyllic + argillic) alteration zones are depicted in white, with the propylitic halo and the unaltered country rocks appearing in a deep blue color. The sand dunes, scattered in the NW–SE direction, are distinguished by a beige hue. As indicated in Supplementary Fig. S2a, a significant portion of the deposit remains uncovered by eolian sands, enabling remote sensing mineral mapping. In the SWIR data, the hydrolytically altered zones are distinctly marked by a crimson hue, whereas the propylitic halo appears in yellowish to pistachio green colors. The unaltered rocks, on the other hand, display a moderate shade of blue (and partly white) forming a distinct contrast to the hydrothermally altered zones (Fig. 3b).

Spectral mineral mapping reveals that a significant portion of the altered zones is comprised of white mica from the phyllic alteration zone (Fig. 3c). The abundance of white mica is notably high in the central parts but sharply declines towards the margins. The minimum wavelength of white mica ranges between 2195 and 2210 nm (Fig. 3d). Notably, the shorter wavelength portion corresponding to Al-rich white mica (appearing bluish in Fig. 3d) is observed towards the core of the system proximal to the mineralized areas. In contrast, the longer wavelength end (varying from yellow to red; Fig. 3d) is found in the distal zones, close to the propylitic alteration. The zones of Al-rich white mica also appear to be dominated by muscovite rather than illite (Fig. 3e), indicating a higher formation temperature proximal to the potassic cores. Assuming that the Al-rich zones are promising exploration targets, besides the known deposits/prospects, the map also highlights new target areas characterized by Al-rich white mica towards the north of the Reko Diq Caldera (marked as A and B in Fig. 3d). These partly covered areas hold potential for further exploration.

The 2350D/2200D ratio map depicted in Fig. 3f shows lower values in the central areas, gradually increasing towards the periphery where the propylitic alteration zone is located. This spatial pattern could be due to the overprinting effect of chlorite's absorption feature at 2340 nm with the Al–OH feature of white mica at 2350 nm (Table 2). The absence of chlorite in the central zone contributes to the low values observed in the ratio map of Fig. 3f, conforming to the zones of Al-rich white micas (Compare Fig. 3d with Fig. 3f). In pixels where white mica is the dominant mineralogy, this ratio might also provide indirect hints about the relative proportions of illite and muscovite, complementing the map shown in Fig. 3e. This is because muscovite exhibits a deeper absorption feature at 2200 nm relative to 2345 nm, resulting in a lower 2348D/2200D ratio when compared to illite.

The mineral kaolinite was mapped as scattered patches outside the hydrothermal systems (Fig. 4a). However, as mentioned below, kaolinite is present in low quantities (i.e., <30 %) in conjunction with white mica in the central zones. The asymmetry of the 2200 nm feature shown in Fig. 4b provides additional evidence for the co-occurrences of kaolinite and white mica. Here, the range of values is between -0.3 and $+0.7$, of which the values $\sim > 0.5$ correspond to kaolinite, values less than 0 are suggestive of Al-poor white mica, and values falling within these ranges indicate a mixture of (Al-rich) white mica with kaolinite.

Chlorite and epidote, as representative minerals of the propylitic alteration, form a circular halo around the Reko Diq crater, marking the outer rim of the hydrothermal systems (Figs. 4c-4f). Towards the northeast, they are elongated and aligned in the NW–SE direction (white arrows in Fig. 5b). The nature of this NW-SE trending anomaly, whether it is linked to the propylitic alteration or attributed to wind-blown sand, remains uncertain and requires further investigation on the ground. Nevertheless, if confirmed to be authentic, it could potentially signify the presence of a concealed hydrothermal system in the northern/northeastern margin of the crater. Furthermore, while the diorite intrusion to the west of the area (Fig. 1) is not reported to be mineralized, it is similarly encircled by the propylitic alteration minerals (marked by a white arrow in Figs. 4e-4f).

When compared, the propylitic zones defined by the Fe–OH feature in Fig. 4c appear narrower and more limited spatially compared to the Mg–OH feature in Fig. 4e. Note that the outcrops of limestone mapped in Fig. 4e are absent in Fig. 4c due to the absence of the 2250 nm feature in carbonates minerals. The mapped limestones conform to the Cretaceous limestone outlined in the geology map in Fig. 1. The minimum wavelengths of the Fe–OH and Mg–OH features range between 2246 and 2261 nm and 2327 to 2345 nm, respectively. If attributed to chlorite only, this is indicative of chlorite of intermediate composition. Note that the calcic outcrops in Figs. 4e-4f display relatively constant wavelength values (i.e., 2331–35 nm). An example of the calcite spectra is illustrated in Fig. 2e.

The epidote, identified by the presence of the 1550 nm absorption

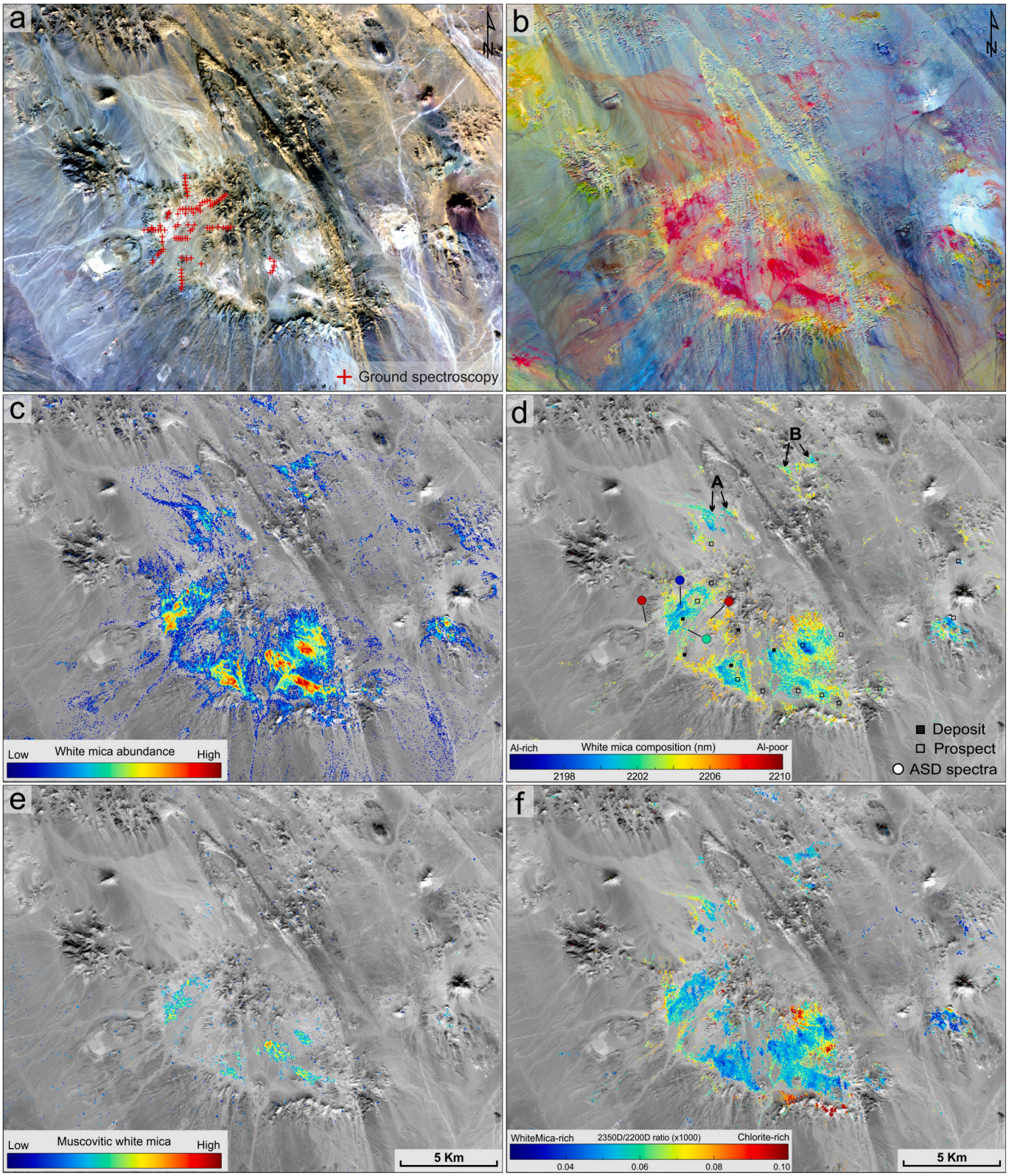

Fig. 3. Alteration mineral maps derived from EnMAP hyperspectral data over the Reko Diq porphyry Cu—Au deposit. The maps in (c) to (f) are color-coded and superimposed onto an albedo image. **a)** EnMAP natural color composite image corresponding to bands at 640, 550, and 460 nm respectively as RGB. **b)** Enhanced false-color composite image using the SWIR bands at 1675, 2208, and 2239 nm respectively as RGB. **c)** White mica abundance map (2200D). **d)** White mica composition map (2200 W). **e)** The distribution of muscovitic white mica. **f)** The ratio between absorption depths at 2340 and 2200 nm (2340D/2200D). The solid circles in (d) represent the ground measurement sites color-coded using the corresponding color bar. The processing methodologies used to generate the illustrated mineral maps are summarized in Table 2. This figure contains modified EnMAP data ©DLR [⟨2022⟩] all rights reserved. (For interpretation of the references to color in this figure legend, the reader is referred to the web version of this article.)

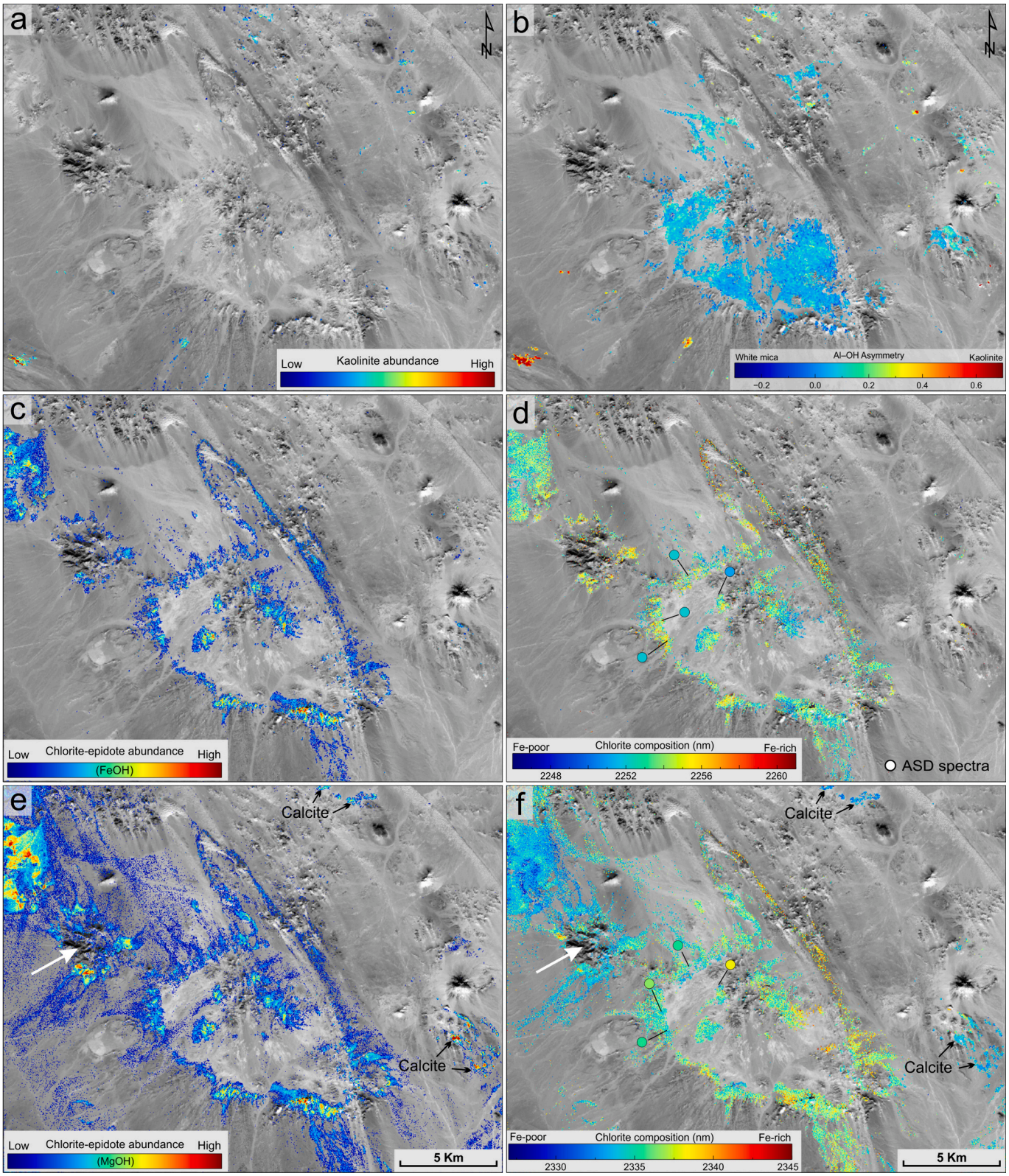

Fig. 4. **a)** Kaolinite abundance based on the 2165 nm absorption feature (2165D). **b)** The asymmetry of the Al–OH absorption feature at 2200 nm derived from the absorption width calculated at 70 % feature depth and smoothed using a median filter. **c)** Chlorite-epidote abundance based on the Fe–OH absorption feature (2250D). **d)** Chlorite composition based on the minimum wavelength of the Fe–OH absorption feature (2250 W). **e)** Chlorite-epidote abundance based on the Mg–OH absorption feature (2340D). **f)** Chlorite composition based on the minimum wavelength of the Mg–OH absorption feature (2340 W). The limestone outcrops are marked by the black arrows. The solid circles in (d) and (f) represent the ground measurement sites color coded using the corresponding color bars. This figure contains modified EnMAP data ©DLR [<2022>] all rights reserved. (For interpretation of the references to color in this figure legend, the reader is referred to the web version of this article.)

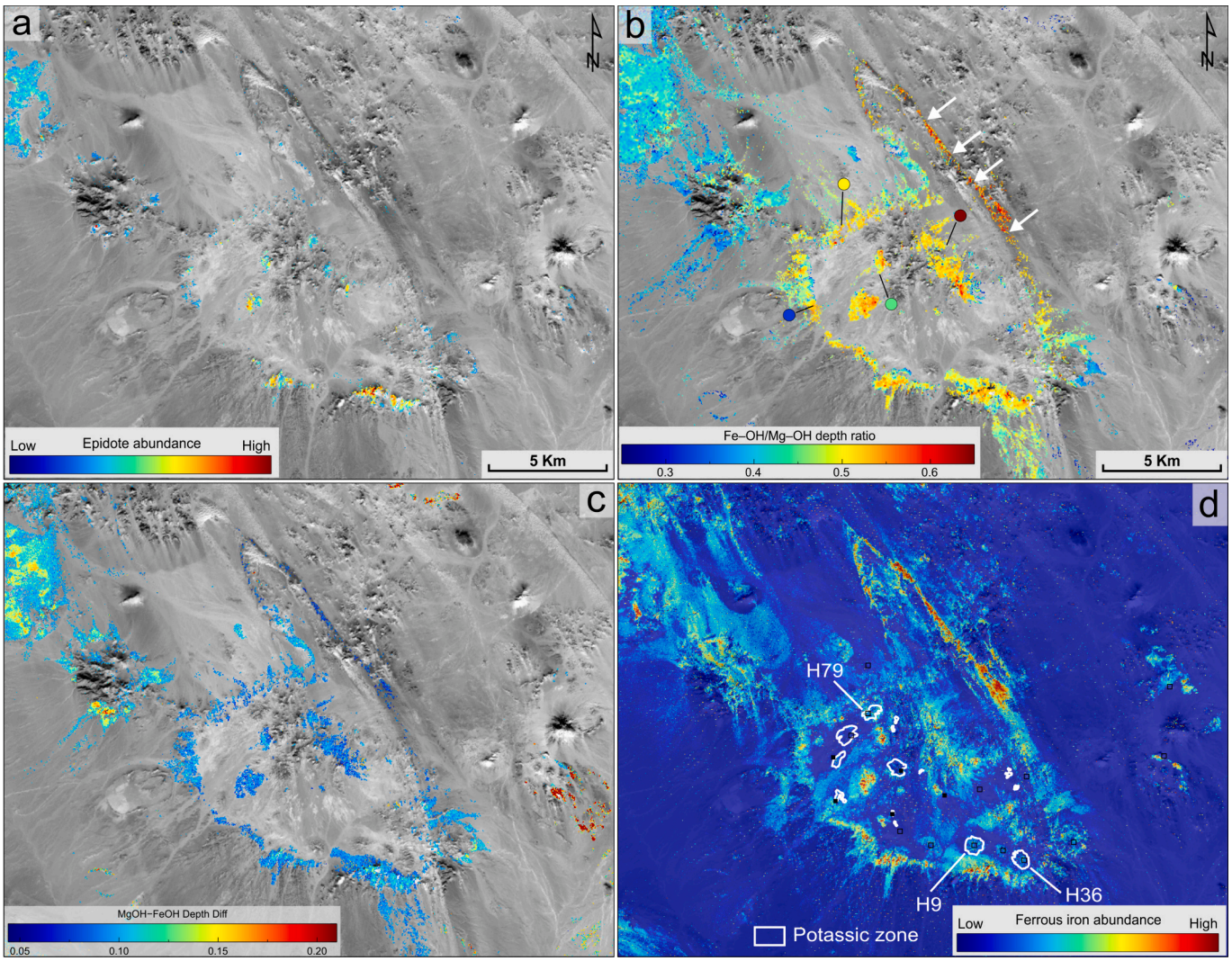

Fig. 5. **a)** Epidote abundance based on the subtle absorption feature at 1550 nm. **b)** the ratio between the absorption depth at 2250 and 2340 nm (Fe–OH/Mg–OH depth ratio). **c)** Depth difference of the chlorite-epidote absorption features at 2250 and 2340 nm. **d)** Ferrous iron abundance. The white arrows in (b) highlight elongated chlorite occurrences discussed in the text. The solid circles represent the ground measurement sites color coded using the corresponding color bars. The outlines of the potassic zones overlaid in (d) are based on field mapping. The processing methodologies used to generate the illustrated mineral maps are summarized in Table 2. This figure contains modified EnMAP data ©DLR [<2022>] all rights reserved. (For interpretation of the references to color in this figure legend, the reader is referred to the web version of this article.)

feature, occurs in a small portion of the propylitic alteration (Fig. 5a). The Fe–OH/Mg–OH ratio map in Fig. 5b, however, reveals a different pattern for epidote occurrences. In this map, values below 0.35 (blue to cyan) can be indicative of epidote (± calcite; see below), while values above 0.6 (dark red) indicate the prevalence of chlorite. Any values falling within this range can be attributed to a mixture of epidote and chlorite (Supplementary Fig. S1a). The depth difference shown in Fig. 5c reveals a similar pattern. Here, the values span between 0.044 and 0.21, of which the higher end ($\sim > 0.2$) corresponds to calcite, values falling between 0.2 and 0.1 to epidote+chlorite, and values below 0.1 to chlorite. The variations depicted in Fig. 5c, however, are more discrete compared to Fig. 5b implying the superiority of the ratio map in Fig. 5b. The pattern derived from the minimum wavelength difference, in contrast, is considerably indistinct and lacks the clarity observed in the maps of depth ratios and depth differences (Supplementary Fig. S2b). Here, the wavelength difference ranges between 66 and 100 nm, which is beyond the limit observed in laboratory data, likely because of mixtures with other minerals.

As illustrated in Fig. 5d, ferrous iron minerals appear to be quite abundant in the area. These minerals are primarily mapped over the propylitic alteration zones in relation to epidote and chlorite minerals. Albeit, they extend into the center partially overlapping with the potassic alteration zones outlined by the white polygons. Ferrous iron, in particular, is pervasive over the potassic cores of the H79, H9, and H36 systems.

The ternary color composite map of calcite, epidote, and chlorite (Fig. 6a) reveals analogous patterns for the propylitic alteration. The red and green hues highlight areas rich in calcite and epidote, respectively, with magenta representing a mixture of calcite + chlorite. A comparison of the maps presented in Figs. 5a-5c and 6a unveils several interesting features. Despite some spatial overlaps between the maps in Fig. 5a and b, there exist clear differences. The most notable difference is the total area recognized to contain epidote, which is significantly larger in Fig. 5b. Another disparity arises from the association of epidote derived from the 1550 nm feature with higher ratio values in Fig. 5b. The mapped minerals in Fig. 6a closely resemble the pattern depicted in the ratio map in Fig. 5b, indicating the potential of this ratio to differentiate between epidote and chlorite within the propylitic alteration zone, though the ratio remain insensitive to calcite co-occurrences. Fig. 6b illustrates the classification results obtained from the SVM method. In

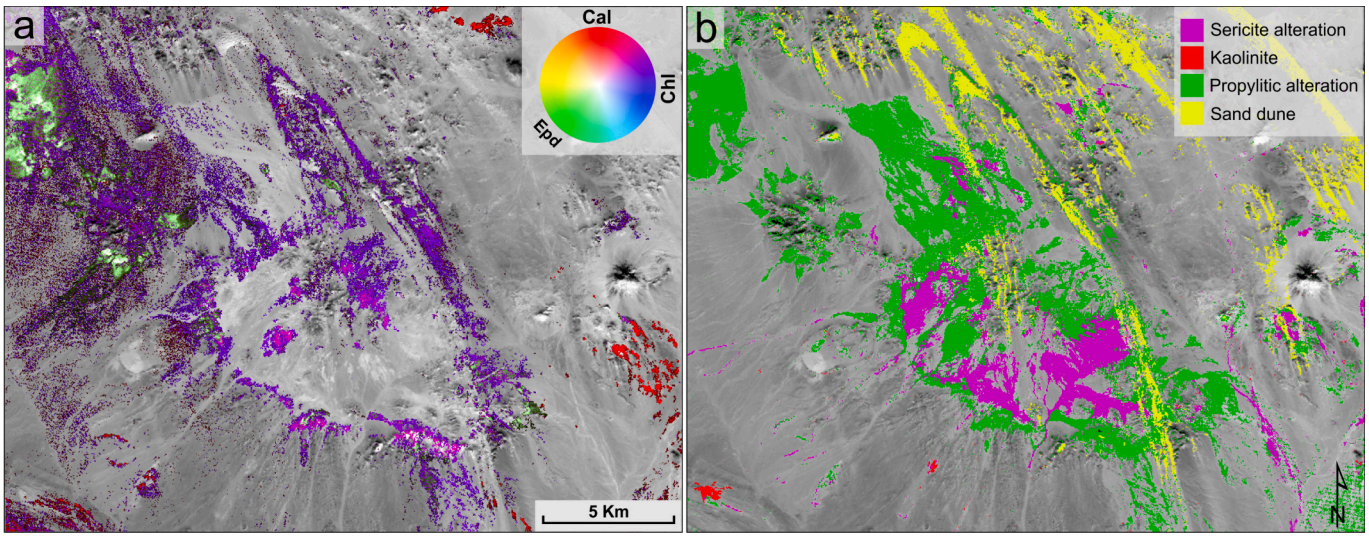

Fig. 6. a) Ternary abundance map derived from the similarity between pixel spectra and a mixed spectral library showing the distribution of calcite (Cal), epidote (Epd), and chlorite (Chl) as RGB. **b)** classification map derived from SVM for the major alteration minerals. This figure contains modified EnMAP data ©DLR [<2022>] all rights reserved. (For interpretation of the references to color in this figure legend, the reader is referred to the web version of this article.)

contrast to the spectroscopic-based methods, SVM was only able to map propylitic and sericite alteration as bulk zones with no ability to distinguish between mineral assemblages. This is likely due to insufficient (and imbalanced) training data for mineral mixtures and the complex (nonlinear) relationships between spectral features and the corresponding mineral classes. While the overall outline of the propylitic alteration in the southern parts is consistent with the maps shown in Fig. 6a, major differences exist over the northern parts.

Secondary sulfate minerals, including jarosite and gypsum, were mapped in small outcrops in the center of the porphyry system (Figs. 7a-7b). These minerals overlap spatially and are mostly concentrated within the phyllic alteration zones. The jarosite-bearing areas largely coincide with the Tanjeel deposit over which supergene enrichment is reported (Perelló et al., 2008), indicating the critical role of pyrite in the process. Yet traces of jarosite are mapped over the H27 and H10 centers. The supergene blankets form due to acid leaching caused by intense pyrite oxidations. While gypsum is being detected across a wider area, it is worth noting that its proportion is expected to be quite low because the 1770 nm feature is weakly developed in the EnMAP data (see also section 5.3). In porphyry systems, gypsum is formed through the hydration of primary anhydrite, which lacks an absorption feature at 1750 nm (Asadzadeh et al., 2023). The presence of gypsum/anhydrite has been confirmed during previous studies (Schmidt, 1976) and in the current field campaign (see section 5.3).

The altered areas are associated with a notable increase in ferric iron contents, particularly over the phyllic alteration zones (Fig. 7c). The ferric iron content is notably high over the Tanjeel deposit where considerable amounts of jarosite are also detected from the SWIR+VNIR bands (Fig. 7a). The wavelengths of the ferric iron features varies between 900 and 960 nm with the shorter wavelengths (i.e., >910 nm in Fig. 7d) corresponding to jarosite-rich areas and the longer wavelengths to goethite zones (compare Fig. 3d with Figs. 7c-7d). Due to EnMAP's noise in this region (see below) and subsequent spectral smoothing, the retrieved minimum wavelengths might not be as accurate as expected.

Fig. 8 shows the scatterplots of the selected spectral parameters used to interpret mineral mixtures in the area. The scatterplot of the absorption feature parameters offers valuable insights into the state of the mineral, composition, and mixtures in the area. In Fig. 8a, the plot of 2200D against 2165D reveals two distinct clusters. The first cluster retaining higher values along both axes is indicative of well-crystalline kaolinite (corresponding to the kaolinite mapped in Fig. 4a). The second cluster, characterized by high values along 2200D and relatively low values along 2165D, corresponds to white mica. The positive correlation between 2200D and 2165D variables in this cluster, running parallel to the kaolinite cluster, suggests that low quantities of kaolinite are present in an intimate mixture with white mica over the deposit. This is further supported by the plot of 2200 W against 2200D in Fig. 8b, where two clusters emerge with no distinct boundary, particularly towards the lower proportions. One cluster, centered around 2205 nm, is close to the wavelength minimum of kaolinite (occurring between 2204 and 2208 nm), indicating the possible presence of kaolinite in the pixels (It should be emphasized that despite the interference of kaolinite's absorption feature, the shifts in the minimum wavelength is largely attributed to changes in the chemistry of white mica). The spectral plots in Figs. 2a-2b demonstrate the subordinate occurrences of kaolinite within white mica-dominated pixels, a point confirmed by field spectroscopy. Note that pixels with high values in the 2165 nm region and low absorption depth at 2200 nm correspond to noise. This applies also to Fig. 8d and e.

The small tail at the right corner of the main cluster in Fig. 8c corresponds to epidote-rich pixels mapped in Fig. 5a. Despite this, however, the overall positive correlation between the two variables indicates that a lower level of epidote is still present in the analyzed pixels (but with no discernible feature at 1550 nm), supporting the earlier finding about the abundance of epidote in the area. The plot in Fig. 8d exhibits a negative correlation between chlorite and white mica in the study area. This is indicative of an intimate mixture between sericitic white mica and chlorite (and likely epidote) and a gradual transition from phyllic to propylitic alteration, represented by white mica and chlorite-epidote, respectively (see also Fig. 3f). It further shows that low quantities of chlorite are still present in the white mica-dominated zones, which increases outward (C.f., Fig. 3f) and vice versa. This notion is corroborated by the spectral plots shown in Fig. 2.

The plot of 2340D against 2250D (Fig. 8e) demonstrates a strong positive correlation between the two parameters. However, towards the higher end, it partitions into two distinct populations: one with deep features at 2340 nm and relatively shallow values at 2250 nm indicative of epidote and the second with deep absorptions at both ranges consistent with chlorite. This trend, observed specifically in pixels where the two minerals are relatively pure, aligns with the pattern observed in Supplementary Fig. S1b. In the EnMAP data, however, due to the pervasive mixture of the two minerals (and mixtures with other minerals including white mica), the clusters blend at lower proportions. This is further exemplified in Fig. 8f, where the Fe–OH feature depth is plotted

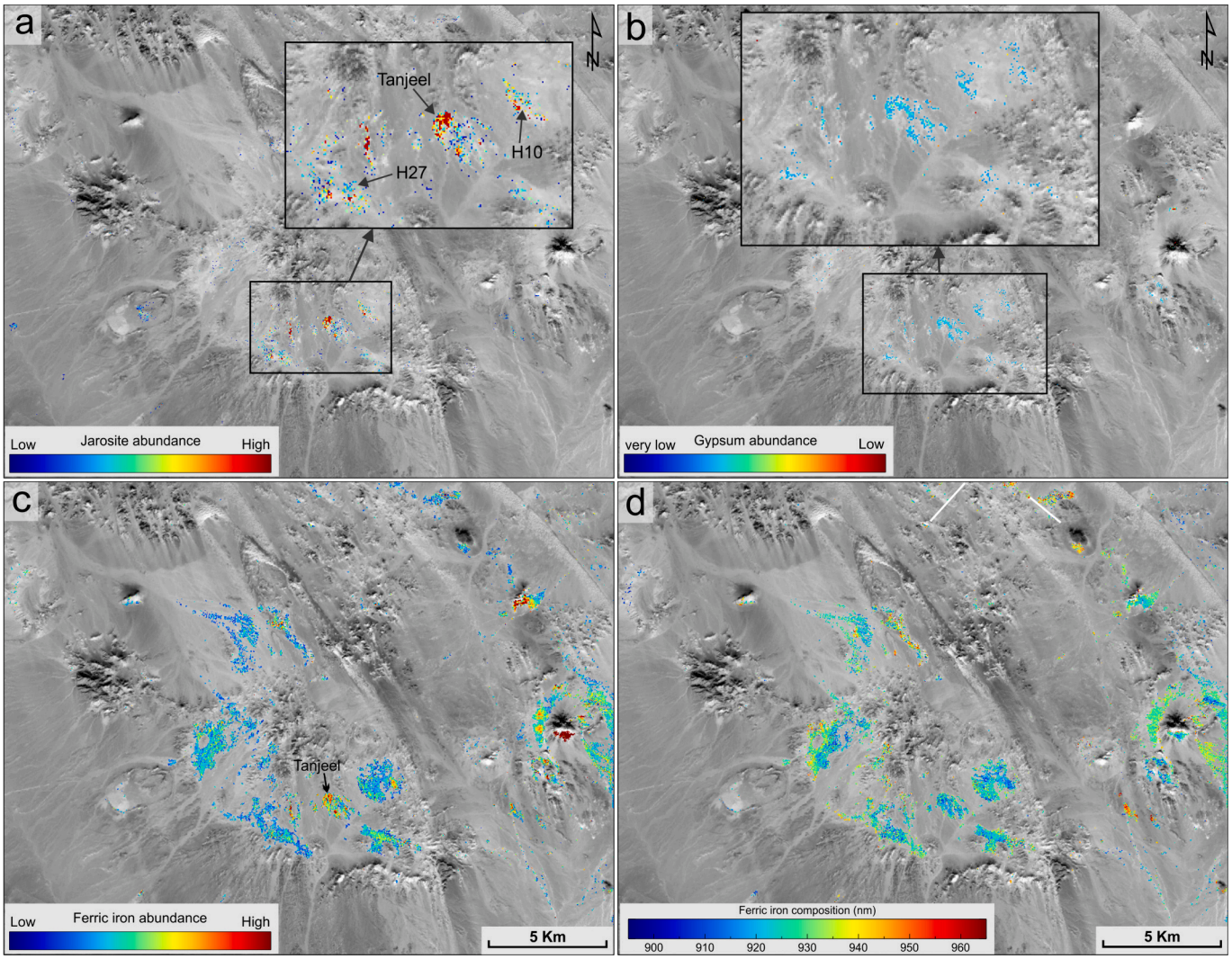

Fig. 7. a) Jarosite abundance based on the Fe–OH feature at 2266 nm. **b)** Gypsum abundance based on the S—O feature at 1750 nm. **c)** Ferric iron abundance (900D). **d)** Ferric iron composition map (900 W). The processing methodologies used to generate the illustrated mineral maps are summarized in Table 2. This figure contains modified EnMAP data ©DLR [<2022>] all rights reserved. (For interpretation of the references to color in this figure legend, the reader is referred to the web version of this article.)

against its minimum wavelength. In this plot, epidote is prominently distinguished by its relatively constant minimum wavelength at ~2254 nm and a deeper absorption feature. At lower proportions, it appears to be mixed with chlorite, which exhibits inherent variability from Fe-poor to Fe-rich species. In other words, except in a limited number of pixels where the two minerals are observed in their isolated/pure forms, in most parts of the area, epidote and chlorite appear to be intimately mixed.

5.3. *Ground spectroscopy and validation of EnMAP results*

Ground spectroscopy revealed similar variations in the composition of white mica ranging between 2197 and 2209 nm (Fig. 9a). Remarkably, the trend and the absolute values derived from ground spectroscopy closely align with the range retrieved from EnMAP data over the entire deposit (Fig. 3d), further validating the accuracy of the EnMAP data and processing methodologies. The shorter wavelengths, K-rich white mica was identified within the phyllic alteration zone surrounding the potassic cores (see the solid circles in Fig. 3d). The mineralogical associations observed by ground spectroscopy were also consistent with those mapped by EnMAP. For instance, the locations dominated by white mica on the ground corresponded to the image data, and areas exhibiting a mixture of chlorite and white mica were consistent between the ground and imagery (Fig. 9a), indicating the intimate mixtures between these minerals. Another subordinate mineral identified on the ground was gypsum, recognized by its characteristic absorption features at 1750 and 1940 nm (Fig. 9b). The secondary absorption feature of muscovite at 2120 nm, detected in the EnMAP data (Fig. 3e), is also clearly discernible in this spectrum. A reasonable agreement was found between the chlorite-epidote absorption features recorded over the propylitic alteration (see Fig. 4d for measurement locality). However, there exist some discrepancies between the data pairs, including the retrieved minimum wavelengths for the Fe–OH and Mg–OH features (Fig. 9c). This could be attributed to the heterogeneity of the propylitic alteration zone and the scaling effects. In the NIR range, however, there is a significant difference between the EnMAP pixel spectrum and ferric iron absorption measured on the ground (Fig. 9d), which is due to the inherent noise of the data in this wavelength range. Following spectral smoothing, the feature appears to closely match the ground data.

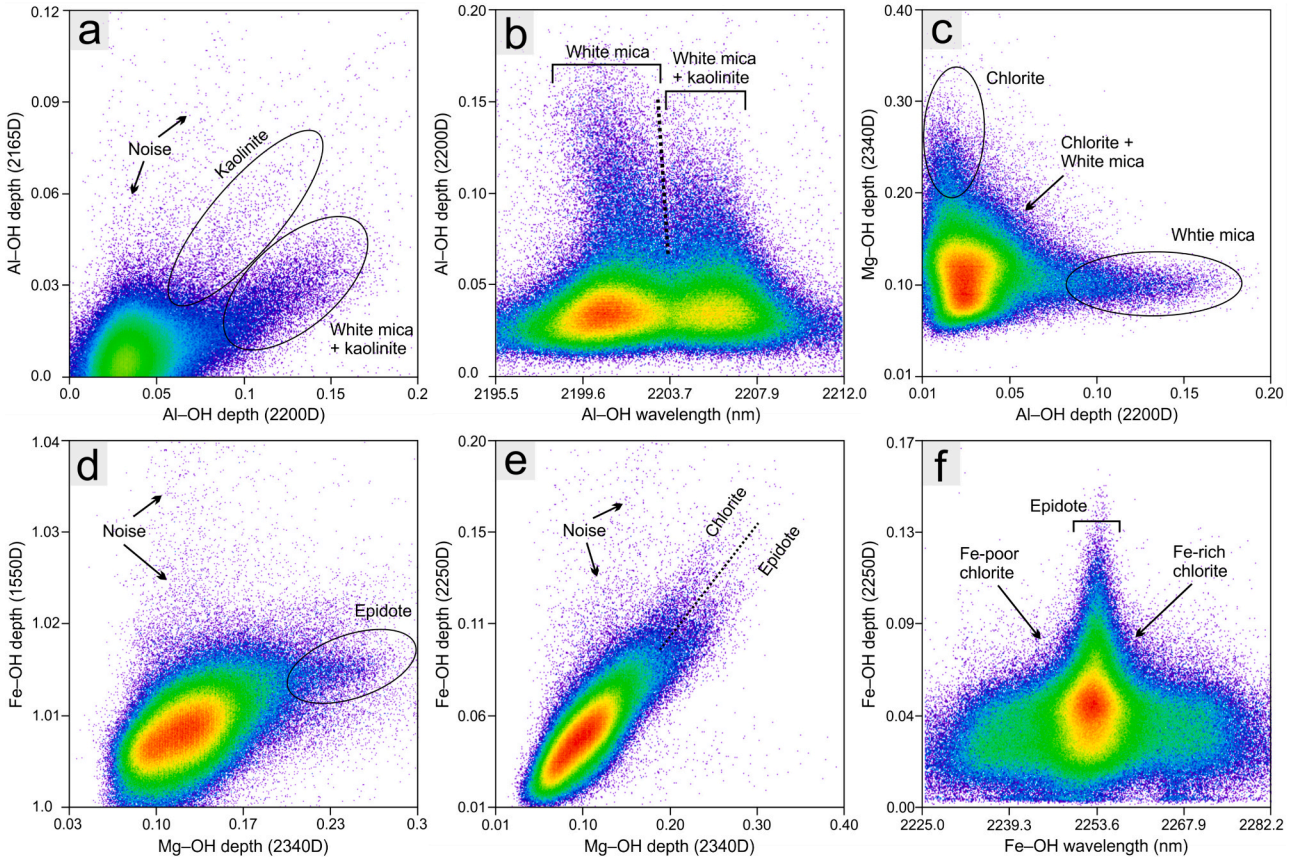

Fig. 8. Scatterplots of the spectral parameters used to decipher mineral mixtures in the Reko Diq area. **a)** The plot of 2200D against 2165D, **b)** 2200 W plotted against 2200D, **c)** Al–OH feature depth plotted against Mg–OH depth at 2340 nm, **d)** the plot of Mg–OH depth (2340D) against epidote's Fe–OH feature at 1550 nm, **e)** the feature depth at 2340 nm plotted against the depth at 2250 nm, and **f)** the Fe–OH minimum wavelength plotted against its depth. The colors show the density of the pixels with a red color corresponding to a higher proportion. (For interpretation of the references to color in this figure legend, the reader is referred to the web version of this article.)

6. Discussion

6.1. Alteration zonation and mineral chemistry

In porphyry systems, the potassic core typically hosts the main body of mineralization (Cooke et al., 2020; Cooke et al., 2014; Sillitoe, 2010). However, except for airborne thermal infrared sensors, remote sensing mapping of potassic alteration presents a significant challenge, primarily because of the low reflectance properties of biotite and the spectral neutrality of K-feldspar in the VNIR–SWIR range. As a result, potassium alteration has been occasionally mapped using airborne imaging spectroscopic data (Asadzadeh et al., 2023). However, as indicated in Fig. 5d, mapping ferrous iron minerals using the NIR bands can provide an alternative approach to detect biotite occurrences indirectly and, consequently, map the potassic zone in exposed porphyry systems. Ferrous iron anomalies can be attributed to Fe^{2+} present in biotite and/or overprinted chlorite minerals associated with potassic alteration.

The zonation pattern observed in Figs. 3c-3e, in which high abundances of Al-rich, muscovitic white mica are proximal to the mineralization centers, is consistent with the typical zoning documented in many other shallow-level porphyry systems using laboratory/field spectroscopy (Alva-Jimenez et al., 2020; Halley et al., 2015; Uribe-Mogollon and Maher, 2018; Wallace and Maher, 2019). It represents the sericite-quartz-pyrite assemblage formed at a high fluid-rock ratio. The composition of white mica typically exhibits vertical and lateral variations within porphyry systems. Vertically, it transitions from phengentic (Al-poor) white mica in the deeper, hotter parts of the deposit to muscovitic (Al-rich) white mica in the upper, cooler parts where potassic alteration forms. Laterally, it varies from high Al contents at the center (<2205 nm in wavelength) to low Al in the distal zones, as is observed in this area and elsewhere (Asadzadeh et al., 2023). The lateral compositional variation is primarily controlled by pH and fluid chemistry and the composition of the host rocks with acidic environments favoring the formation of muscovite white mica. Such remotely detectable variations arise from Tschermak substitution, in which octahedral and tetrahedral Al^{3+} are substituted by Fe^{2+}/Mg^{2+} and Si^{4+} cations, respectively (Halley et al., 2015; Uribe-Mogollon and Maher, 2018; van Ruitenbeek et al., 2012).

In the Reko Diq area, while the majority of exploration efforts have been focused on the western porphyry centers, the white mica composition map in Fig. 3d reveals that the eastern centers are equally prospective for copper mineralization and warrant additional drilling. Similarly, the anomalies located north of the crater represent valuable targets for field investigation and sampling.

The progressive decline in thermal conditions and flow dynamics within the porphyry hydrothermal system, combined with paleosurface erosion can give rise to distinct overprinting (telescoping) of the initial alteration zones (Sillitoe, 2010). In the Reko Diq area, white mica is found to be spatially associated (and spectrally mixed) with kaolinite and chlorite (see Figs. 8a, c, and 2a,b). This pervasive mixing can be attributed to the overprinting of initial phyllic alteration by a subsequent low-temperature intermediate argillic alteration, forming a kaolinite-illite-chlorite assemblage (Halley et al., 2015; Sillitoe, 2010). The detection of only trace amounts of kaolinite over the porphyry systems implies that either the pH of the fluid was not very acidic (>4) or the circulation of acidic fluids did not endure for a long time. The

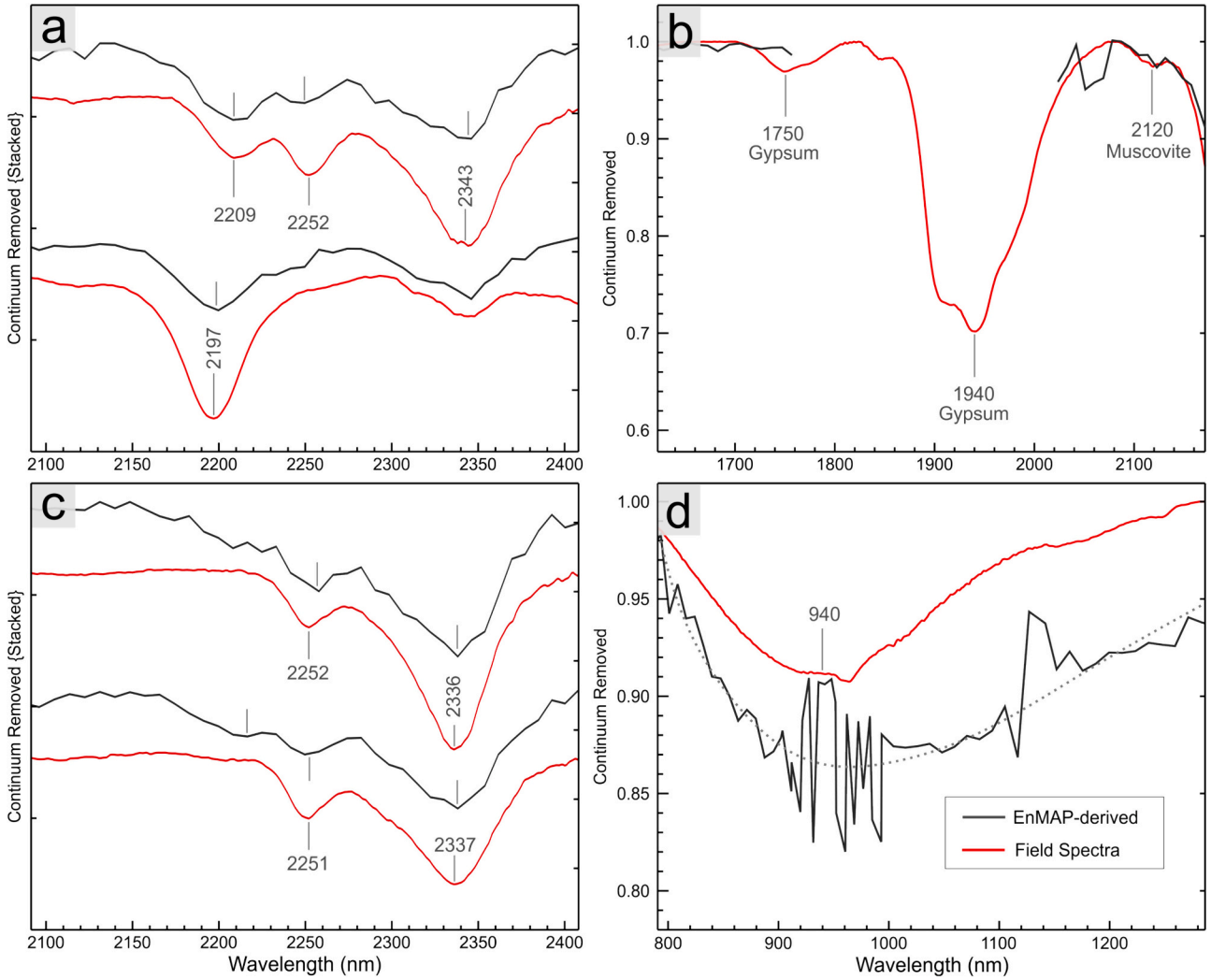

Fig. 9. The EnMAP pixel spectra (solid gray lines) compared to ground spectroscopic data obtained from an ASD instrument: **a)** variations in the compositions of white mica (± chlorite), **b)** the same spectra as (a) exhibited between 1650 and 2140 nm, to highlight the absorption features of gypsum at 1750 and 1940 nm, **c)** chlorite and epidote spectra from the propylitic alteration zone, **d)** the broad ferric iron feature in the NIR, indicating the noisy nature of the EnMAP data within this range. For clarity, the spectrally smoothed data is represented by the dashed line in (d). The locations of the samples are shown in Figs. 3d and 4d. This illustration contains modified EnMAP data ©DLR [⟨2002⟩].

relatively abundant chlorite inside the phyllic zone, which is detectable remotely, supports the former assumption. Here, chlorite is the retrograde of the original mafic minerals (Sillitoe, 2010). The pronounced level of chlorite at the margins of the phyllic zone (Fig. 3f), which is accompanied by Al-poor, texture-destructive illite (Fig. 3d), indicates the progressive cooling and neutralization of the hot acidic fluid while passing from sericite to inner propylitic alteration. The coexistence of chlorite with Al-poor white mica within this zone, is suggestive of the texture-destructive illite in the periphery of the system.

In spectral geology, smectites are commonly separated from white mica (illite-muscovite), but there has been little attempt to distinguish between illite and sericite (muscovite). In contrast to sericite, illite forms during the intermediate argillic alteration at lower temperature conditions and has less association with mineralization processes. Accordingly, differentiating between illite and sericite can offer valuable proximity to the heat and fluid sources within the system. The use of the 2120 nm absorption feature in this study yielded very encouraging results. However, the method (and the spectral index) should be further tested in analogous hydrothermal systems before being used as an index to differentiate the mineralogy of white mica.

A question that arises here is to which degree the white mica compositional map depicted in Fig. 3d, is interfered by the simultaneous occurrences of kaolinite. A linear mixture simulation using the USGS spectral library showed that the existence of 50 % kaolinite in a pixel (with its minimum at 2204 nm) can shift the minimum wavelength of white mica from 2202 to 2204 nm. At the 30 % level, it shifts the minimum to just 1 nm. While this implies that the presence of kaolinite can interfere with the minimum wavelength mapping of white mica, for low quantities of kaolinite (i.e., <30 %) observed in this particular area, the shift remains on the order of 1 nm. In other words, despite being overprinted by kaolinite, the variations mapped in Fig. 3d are mostly due to inherent compositional variations in hydrothermally-formed white mica.

6.2. *Differentiation of calcite, epidote, and chlorite*

A common spatial pattern in porphyry systems is zonation in the propylitic alteration, characterized by a transition outward from actinolite to epidote to chlorite. Chlorite, as the dominant alteration mineral within the propylitic zone, typically exhibits lateral variations in its composition, with Mg-rich chlorite appearing in the inner parts due to higher fluid temperature and more oxidized and acidic fluids proximal

to the intrusive center (Asadzadeh et al., 2023; Cooke et al., 2014; Neal et al., 2018). This characteristic zonation pattern, however, is not clearly evident in Fig. 4d and f. The lack of clear zoning may be attributed to the spatial and temporal overlap of multiple magmatic-hydrothermal events in the Reko Diq crater, coupled with successive stages of epidote formation and dissolution resulting in pronounced overprinting of alteration assemblages (Fig. 8f and c). The end result is an intimate mixing of underlying minerals, obscuring the inherent variation in the minimum wavelength (composition) of chlorite.

Our spectral simulations also showed that white mica's features at 2200 and 2345 nm can contribute to shifting the absorption minimums of chlorite. At 50 % proportion, it causes the Fe–OH feature to shift from 2252 to 2246 nm and from 2246 to 2238 nm and the Mg–OH feature from 2335 to 2344 nm and from 2321 to 2333 nm for Fe-rich and Fe-poor chlorites, respectively. In other words, the Mg–OH and Fe–OH features of chlorite are respectively shifted towards shorter and longer wavelengths when they are overlapped by white mica features. Physical mixtures of chlorite with epidote and calcite showed a similar pattern. At 60 % (30 %) relative proportion, epidote can shift the minimum wavelength of chlorite from 2346 to 2339 (2341) nm. Calcite can induce change from 2346 to 2342 and 2344 nm at 60 % and 30 % relative proportions, respectively. Yet both minerals have little effect on the Fe–OH absorption feature at 2255 nm. The absorption minimums of the epidote are relatively constant occurring at 2254–2255 and 2337–2338 nm. Such mixture-induced shifts in the minimum wavelengths of chlorite likely have hindered compositional mapping using EnMAP data and can explain the absence of discernible patterns within the propylitic zones (Fig. 4d and f); although heterogeneity in the composition of the host rock surrounding the volcanic crater (Fig. 1) may have played a role. The minimum wavelength of chlorite in this area typically falls between 2250 and 2256 nm, which is typical of intermediate chlorite composition.

In the literature, the separation of epidote from chlorite typically relies on epidote's diagnostic feature at 1550 nm (Cudahy et al., 2008a; Roache et al., 2011). However, as indicated in Fig. 5a, this method can underestimate the spatial extent of epidote for several reasons: (i) the feature is inherently weak and its spectral contrast compared to sensor noise level is low; thus many of the epidote-bearing pixels could go undetected. The EnMAP sensor, in particular, cannot reliably retrieve the left shoulder of this feature due to the low SNR of the corresponding bands (highlighted in Fig. 2d) and the remaining atmospheric noise at the edge of the 1400 nm water absorption. (ii) The intensity of the absorption feature is negatively affected by chlorite cooccurrence. As depicted in Fig. 10, the existence of 20 % chlorite in a sample results in a 50 % reduction in the intensity of this absorption feature. (iii) the shift in the composition from epidote to clinozoisite (Roache et al., 2011) can reduce the intensity and thus its detectability with clinozoisite showing less pronounced absorption features. So by using this feature, epidote is detectable only when it is highly abundant and is not associated with large amounts of chlorite. This could explain the sparse occurrences of epidote mapped in Fig. 5a using the 1550 nm feature.

On the other hand, the absorption depth index (2250D/2340D) proposed in this study was proved to be a useful index in distinguishing between epidote and chlorite and predicting the mixtures between them in the EnMAP data (Fig. 5b and Supplementary Fig. S1b). Although it is not directly sensitive to calcite occurrences in a pixel, which is predicted in Fig. 6a to coexist with epidote. Note that the mixture library reported by Dalton et al. (2004), used to generate Fig. 6a, contains Fe-rich clinochlore with its minimum wavelength at 2346 nm, which is much beyond the trend mapped in this area (Fig. 4f). Accordingly, it is likely that many of the chlorite+calcite areas mapped in Fig. 6a (magenta color) correspond to Fe-poor chlorite that in the absence of a representative endmember in the library, are mapped as chlorite+calcite mixture.

6.3. Comparison with ASTER mineral maps

A comparison between the results of this study and the mineral maps obtained from processing the ASTER multispectral data in Rowan et al. (2006) reveals several notable differences: (i) in contrast to ASTER, EnMAP detected no occurrences of alunite in the area; (ii) while both sensors successfully detected jarosite, the map derived from EnMAP using the combined VNIR+SWIR bands was spatially more coherent; (iii) EnMAP data outlines a larger expanse of white mica within the phyllic alteration zones, and (iv) EnMAP accurately captures the complete shape of the propylitic alteration zone while discriminating between epidote, chlorite, and calcite minerals. Furthermore, EnMAP provides valuable insights into the composition and mineralogy of white mica, the overprint of kaolinite, illite, and chlorite on the sericite alteration assemblages, the presence of gypsum/anhydrite-rich zones, and the distribution of ferric and ferrous iron minerals. The capability of EnMAP to reveal the chemistry of vector minerals, which has not been possible in multispectral datasets like ASTER, can serve as a useful tool for identifying the intrusive centers of the porphyry system and discriminating between barren and fertile phyllic zones. The capability of EnMAP in characterizing the mineralogy of propylitic alteration can

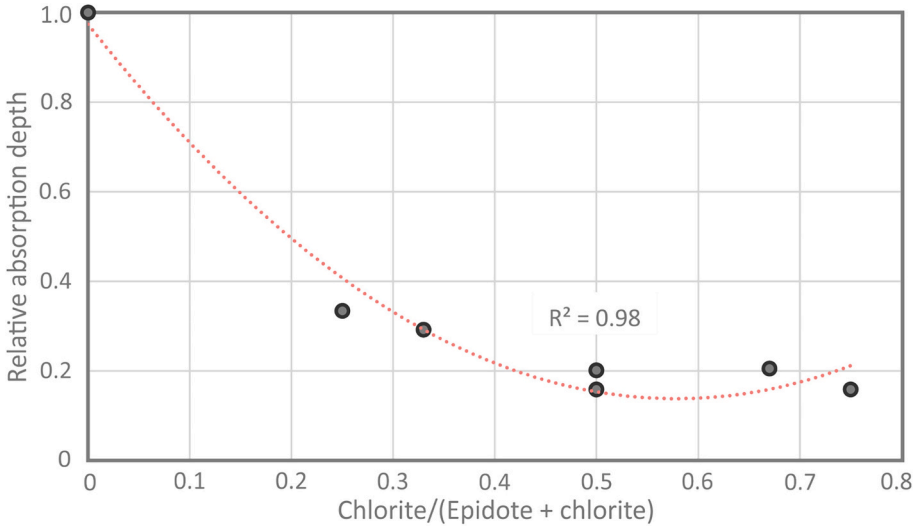

Fig. 10. The relative depth of the 1540 nm absorption feature of epidote as a function of chlorite proportion calculated using the USGS spectral library of chlorite-epidote mixtures described in Dalton et al. (2004).

also be highly valuable for identifying exploration targets within green rocks (Pacey et al., 2020).

Overall, the mineral maps derived from EnMAP data exhibit greater spatial coherence compared to ASTER data and reveal a wealth of new information about the mineralogy of the alteration assemblages. Nonetheless, EnMAP has a narrow swath width (i.e., 30 × 30 km) and is therefore useful for studying targets of small spatial extent. The next generation of imaging spectroscopic missions currently in development, including ESA's Copernicus Hyperspectral Imaging Mission for the Environment (CHIME) and NASA's Biology and Geology (SBG) missions, will be able to provide wide swath coverages (120–180 km) enabling regional to continental mineral mapping.

6.4. Spectral processing method

In terms of the processing method, quadratic fitting to the minimum was found to be susceptible to sensor noise, particularly towards the longer wavelength range of the SWIR detector, where calcite-chlorite-epidote's absorption features occur. The method also proved impractical for mapping ferric iron absorption in the VNIR. Conversely, higher-order polynomial fitting, which incorporates more bands in the retrieval process, demonstrated greater resilience against noise and provided more spatially coherent results for chlorite, epidote, and calcite, while exhibiting a notably lower level of retrieval uncertainty. For instance, a 4th-order polynomial fitting can attain an uncertainty of <2.4 nm in the retrieval process (Asadzadeh and Souza Filho, 2016), which is lower than the 3.8 nm uncertainty reported in Rodger et al. (2012) for the quadratic fitting method. This technique, however, struggled to yield satisfactory estimates for ferric iron abundance/composition, mostly due to the VNIR–SWIR sensor overlap at this wavelength range, the noisy channels at the edge of the VNIR detector (Storch et al., 2023), and likely residual atmospheric artifacts.

The polynomial fitting technique, as a physically-based approach stemming from spectroscopic principles for processing imaging spectroscopic data at the individual pixel level, is sensor agnostic and transferable to other areas/scales, ensuring reproducible results using EnMAP and other hyperspectral datasets. Leveraging the spectral knowledge about minerals eliminates the need for training data in the detection and mapping process. The method presented here, involving interactive thresholding of the retrieved spectral parameters using scatterplots, can further improve the mineral identification process while providing useful information about mineral mixtures, their relative abundances, and compositional variations without the need for reference data. The level of information presented in this study cannot be obtained using standard classification algorithms without high-quality training data.

7. Conclusion

By leveraging the spectroscopic contents of EnMAP data, more than nine mineral products were identified, mapped, and verified across the Reko Diq mining district. These include white micas, chlorite, epidote, calcite, kaolinite, gypsum, and jarosite, as well as ferric and ferrous iron minerals. The chemical composition of white mica, inferred from variations in the minimum wavelength of the 2200 nm feature, proved valuable in unveiling the geochemical/thermal gradients of the magmatic-hydrothermal fluids, providing an effective vectoring tool towards the mineralized centers; a characteristic not feasible by multispectral datasets. The spectroscopic-based processing method also revealed a late-stage overprint of kaolinite (and illite) on the sericite alteration assemblages, a transition from highly abundant muscovite in the center to chlorite outwards, and a mixture of epidote, chlorite, and calcite within the propylitic alteration zone. Furthermore, the ferrous iron mineral map was found to effectively highlight the potassic alteration zones, offering a potentially new way for mapping this important alteration using imaging spectroscopic data.

Overall, this study demonstrated the superior quality and good calibration accuracy of EnMAP hyperspectral data and its effectiveness in delineating the architecture, zonation, overprinting relationships, and physicochemistry of the alteration minerals associated with the porphyry copper deposit. The accurate mineralogical information and the enhanced mapping capability provided by this instrument is expected to play a significant role in discovering new deposits in well-exposed metallogenic belts worldwide, facilitating ore targeting and prospect appraisal.

CRediT authorship contribution statement

Saeid Asadzadeh: Writing – review & editing, Writing – original draft, Visualization, Validation, Software, Methodology, Investigation, Formal analysis, Data curation, Conceptualization. **Xiaodong Zhou:** Writing – review & editing, Validation, Methodology. **Sabine Chabrillat:** Writing – review & editing, Supervision, Resources, Project administration, Funding acquisition.

Declaration of competing interest

The authors declare the following financial interests/personal relationships which may be considered as potential competing interests.

Saeid Asadzadeh reports financial support was provided by the EnMAP science program (grant number 50EE1923 and 50EE2401).

Data availability

The authors can not share the data, but EnMAP data are freely available via the portal of the instrument via the portal of the instrument at www.enmap.org.

Acknowledgment

This study was supported by the EnMAP science program (grant numbers 50EE1923 and 50EE2401) under the DLR Space Agency with resources from the German Federal Ministry for Economic Affairs and Climate Action. The authors wish to thank Barrick Gold Corporation for permission to publish the Reko Diq spectral results and acknowledge Julian Aldridge for collecting the field spectral data. The EnMAP data are licensed products of DLR [2022], all rights reserved.

Appendix A. Supplementary data

Supplementary data to this article can be found online at https://doi.org/10.1016/j.rse.2024.114389.

References

Alonso, K., Bachmann, M., Burch, K., Carmona, E., Cerra, D., de los Reyes, R., Dietrich, D., Heiden, U., Hölderlin, A., Ickes, J., Knodt, U., Krutz, D., Lester, H., Müller, R., Pagnutti, M., Reinartz, P., Richter, R., Ryan, R., Sebastian, I., Tegler, M., 2019. Data products, quality and validation of the DLR earth sensing imaging spectrometer (DESIS). Sensors 19, 4471.

Alva-Jimenez, T., Tosdal, R.M., Dilles, J.H., Dipple, G., Kent, A.J.R., Halley, S., 2020. Chemical variations in hydrothermal White Mica across the Highland Valley porphyry cu-Mo District, British Columbia, Canada. Econ. Geol. 115, 903–926.

Asadzadeh, S., Souza Filho, C.R., 2016. Iterative curve fitting: A robust technique to estimate the wavelength position and depth of absorption features from spectral data. IEEE Trans. Geosci. Remote Sens. 54, 5964–5974.

Asadzadeh, S., Filho, Souza, C.R.D, Nanni, M.R., Batezelli, A., 2019. Multi-scale mapping of oil-sands in Anhembi (Brazil) using imaging spectroscopy. Int. J. Appl. Earth Obs. Geoinf. 82, 101894.

Asadzadeh, S., Chabrillat, S., Cudahy, T., Rashidi, B., Souza Filho, C.R., 2023. Alteration Mineral Mapping of the Shadan Porphyry cu–au Deposit (Iran) Using Airborne Imaging Spectroscopic Data: Implications for Exploration Drilling. Economic Geology, Accepted.

Bedini, E., 2017. The use of hyperspectral remote sensing for mineral exploration: a review. J. Hyperspect. Remote Sens. 7, 23.

Berger, B.R., King, T.V.V., Morath, L.C., Phillips, J.D., 2003. Utility of high-altitude infrared spectral data in mineral exploration: application to northern Patagonia Mountains, Arizona. Econ. Geol. 98, 1003–1018.
Chabrillat, S., Guanter, L., Kaufmann, H., Foerster, S., Beamish, A., Brosinsky, A., Wulf, H., Asadzadeh, S., Bochow, M., Bohn, N., Boesche, N., Bracher, A., Brell, M., Buddenbaum, C.D.H., Fischer, S., Hank, T., Heiden, U., Heim, B., Heldens, W., Hill, J., Hollstein, A., Hostert, P., Krasemann, H., LaPorta, L., Leitão, P.J., van der Linden, S., Mauser, W., Milewski, R., Mottus, M., Okujeni, A., Oppelt, N., Pinnel, N., Roessner, S., Röttgers, R., Schneiderhan, T., Schickling, A., Soppa, M., Staenz, K., Segl, K., 2022. EnMAP Science Plan. In: EnMAP Technical Report. GFZ Data Services, Potsdam, p. 88.
Chirico, R., Mondillo, N., Laukamp, C., Mormone, A., Di Martire, D., Novellino, A., Balassone, G., 2023. Mapping hydrothermal and supergene alteration zones associated with carbonate-hosted Zn-Pb deposits by using PRISMA satellite imagery supported by field-based hyperspectral data, mineralogical and geochemical analysis. Ore Geol. Rev. 152, 105244.
Clark, R.N., Swayze, G.A., Livo, K.E., Kokaly, R.F., Sutley, S.J., Dalton, J.B., McDougal, R. R., Gent, C.A., 2003. Imaging spectroscopy: earth and planetary remote sensing with the USGS Tetracorder and expert systems. J. Geophys. Res.: Planet. 108.
Cogliati, S., Sarti, F., Chiarantini, L., Cosi, M., Lorusso, R., Lopinto, E., Miglietta, F., Genesio, L., Guanter, L., Damm, A., Pérez-López, S., Scheffler, D., Tagliabue, G., Panigada, C., Rascher, U., Dowling, T.P.F., Giardino, C., Colombo, R., 2021. The PRISMA imaging spectroscopy mission: overview and first performance analysis. Remote Sens. Environ. 262, 112499.
Cooke, D.R., Hollings, P., Wilkinson, J.J., Tosdal, R.M., 2014. 13.14 - geochemistry of porphyry deposits. In: Holland, H.D., Turekian, K.K. (Eds.), Treatise on Geochemistry, Second edition. Elsevier, Oxford, pp. 357–381.
Cooke, D.R., Agnew, P., Hollings, P., Baker, M., Chang, Z., Wilkinson, J.J., Ahmed, A., White, N.C., Zhang, L., Thompson, J., Gemmell, J.B., Danyushevsky, L., Chen, H., 2020. Recent advances in the application of mineral chemistry to exploration for porphyry copper–gold–molybdenum deposits: detecting the geochemical fingerprints and footprints of hypogene mineralization and alteration. Geochem.: Explorat. Environ. Analy. 20, 176–188.
Coulter, D.W., Zhou, X., Wickert, L.M., & Harris, P.D. (2017). Advances in Spectral Geology and Remote Sensing: 2008–2017. V. Tschirhart, & M.D. Thomas (Eds.), Sixth Decennial International Conference on Mineral Exploration (23–50): Proceedings of Exploration 17.
Cudahy, T., 2016. Mineral mapping for exploration: an Australian journey of evolving spectral sensing technologies and industry collaboration. Geosciences 6, 52.
Cudahy, T.J., Wilson, J., Hewson, R., Linton, P., Harris, P., Sears, M., Okada, K., Hackwell, J.A., 2001. Mapping porphyry-skarn alteration at Yerington, Nevada, using airborne hyperspectral VNIR-SWIR-TIR imaging data. In: IGARSS 2001. Scanning the Present and Resolving the Future. Proceedings. IEEE 2001 International Geoscience and Remote Sensing Symposium (Cat. No.01CH37217), 632, pp. 631–633.
Cudahy, T., Jones, M., Thomas, M., Laukamp, C., Caccetta, M., Hewson, R., Rodger, A., Verral, M., 2008a. Next generation mineral mapping: Queensland airborne HyMap and satellite ASTER surveys 2006-2008. In: CSIRO Exploration & Mining Report P2007 / 364.
Cudahy, T.J., Jones, M., Thomas, M., Laukamp, C., Caccetta, M., Hewson, R., Rodger, A., Verrall, M., 2008b. Next generation mineral mapping: Queensland airborne HyMap and satellite ASTER surveys 2006-2008. In: CSIRO Exploration & Mining Report P2007 / 364, p. 152.
Dalton, J.B., Bove, D.J., Mladinich, C.S., Rockwell, B.W., 2004. Identification of spectrally similar materials using the USGS Tetracorder algorithm: the calcite–epidote–chlorite problem. Remote Sens. Environ. 89, 455–466.
Di Tommaso, I., Rubinstein, N., 2007. Hydrothermal alteration mapping using ASTER data in the Infiernillo porphyry deposit, Argentina. Ore Geol. Rev. 32, 275–290.
Dong, X., Gan, F., Li, N., Zhang, S., Li, T., 2022. Mineral mapping in the Duolong porphyry and epithermal ore district, Tibet, using the Gaofen-5 satellite hyperspectral remote sensing data. Ore Geol. Rev. 151, 105222.
Duke, E.F., 1994. Near infrared spectra of muscovite, Tschermak substitution, and metamorphic reaction progress: implications for remote sensing. Geology 22, 621–624.
Energy, U.S.D.o, 2023. Critical Materials Assessment.
Goetz, A.F.H., Rock, B.N., Rowan, L.C., 1983. Remote sensing for exploration; an overview. Econ. Geol. 78, 573–590.
Graham, G.E., Kokaly, R.F., Kelley, K.D., Hoefen, T.M., Johnson, M.R., Hubbard, B.E., 2018. Application of imaging spectroscopy for mineral exploration in Alaska: A study over porphyry cu deposits in the eastern Alaska range. Econ. Geol. 113, 489–510.
Green, R.O., 2022. The NASA Earth Venture Instrument, Earth Surface Mineral Dust Source Investigation (EMIT). In: IGARSS 2022–2022 IEEE International Geoscience and Remote Sensing Symposium, pp. 5004–5006.
Guanter, L., Kaufmann, H., Segl, K., Foerster, S., Rogass, C., Chabrillat, S., Kuester, T., Hollstein, A., Rossner, G., Chlebek, C., Straif, C., Fischer, S., Schrader, S., Storch, T., Heiden, U., Mueller, A., Bachmann, M., Mühle, H., Müller, R., Habermeyer, M., Ohndorf, A., Hill, J., Buddenbaum, H., Hostert, P., Van der Linden, S., Leitão, P.J., Rabe, A., Doerffer, R., Krasemann, H., Xi, H., Mauser, W., Hank, T., Locherer, M., Rast, M., Staenz, K., Sang, B., 2015. The EnMAP Spaceborne imaging spectroscopy Mission for earth observation. Remote Sens. 7, 8830–8857.
Halley, S., Dilles, J.H., Tosdal, R.M., 2015. Footprints: hydrothermal alteration and geochemical dispersion around porphyry copper deposits. SEG Discover. 1–17.
Kokaly, R.F., Clark, R.N., Swayze, G.A., Livo, K.E., Hoefen, T.M., Pearson, N.C., Wise, R. A., Benzel, W., Lowers, H.A., Driscoll, R.L., Klein, A.J., 2017. USGS spectral library version 7. In: Data Series, p. 68. Reston, VA.
Kruse, F.A., Boardman, J.W., Huntington, J.F., 2003. Comparison of airborne hyperspectral data and EO-1 Hyperion for mineral mapping. IEEE Trans. Geosci. Remote Sens. 41, 1388–1400.
Laukamp, C., Rodger, A., LeGras, M., Lampinen, H., Lau, I.C., Pejcic, B., Stromberg, J., Francis, N., Ramanaidou, E., 2021. Mineral Physicochemistry underlying feature-based extraction of mineral abundance and composition from shortwave, mid and thermal infrared reflectance spectra. Minerals 11, 347.
Liu, Y.N., Sun, D.X., Hu, X.N., Ye, X., Li, Y.D., Liu, S.F., Cao, K.Q., Chai, M.Y., Zhou, W.Y. N., Zhang, J., Zhang, Y., Sun, W.W., Jiao, L.L., 2019. The advanced hyperspectral imager: aboard China's GaoFen-5 satellite. IEEE Geosci. Remote Sens. Magaz. 7, 23–32.
Mars, J.C., 2018. Mineral and lithologic mapping capability of WorldView 3 data at mountain pass, California, using true- and false-color composite images, band ratios, and logical operator algorithms. Econ. Geol. 113, 1587–1601.
Mars, J.C., Rowan, L.C., 2006. Regional mapping of phyllic- and argillic-altered rocks in the Zagros magmatic arc, Iran, using advanced Spaceborne thermal emission and reflection radiometer (ASTER) data and logical operator algorithms. Geosphere 2, 161–186.
Matsunaga, T., Iwasaki, A., Tachikawa, T., Tanii, J., Kashimura, O., Mouri, K., Inada, H., Tsuchida, S., Nakamura, R., Yamamoto, H., Iwao, K., 2022. The Status and Early Results of Hyperspectral Imager Suite (HISUI). In: IGARSS 2022–2022 IEEE International Geoscience and Remote Sensing Symposium, pp. 5399–5400.
Neal, L.C., Wilkinson, J.J., Mason, P.J., Chang, Z., 2018. Spectral characteristics of propylitic alteration minerals as a vectoring tool for porphyry copper deposits. J. Geochem. Explor. 184, 179–198.
Pacey, A., Wilkinson, J.J., Cooke, D.R., 2020. Chlorite and epidote mineral chemistry in porphyry ore systems: A case study of the Northparkes District, New South Wales, Australia. Econ. Geol. 115, 701–727.
Perelló, J., Razique, A., Schloderer, J., Asad-ur-Rehman, 2008. The Chagai porphyry Copper Belt, Baluchistan Province, Pakistan. Econ. Geol. 103, 1583–1612.
Portela, B., Sepp, M.D., van Ruitenbeek, F.J.A., Hecker, C., Dilles, J.H., 2021. Using hyperspectral imagery for identification of pyrophyllite-muscovite intergrowths and alunite in the shallow epithermal environment of the Yerington porphyry copper district. Ore Geol. Rev. 131, 104012.
Pour, A.B., Hashim, M., 2012. The application of ASTER remote sensing data to porphyry copper and epithermal gold deposits. Ore Geol. Rev. 44, 1–9.
Razique, A., Tosdal, R.M., Creaser, R.A., 2014. Temporal evolution of the Western porphyry cu-au Systems at Reko Diq, Balochistan, Western Pakistan*. Econ. Geol. 109, 2003–2021.
Roache, T.J., Walshe, J.L., Huntington, J.F., Quigley, M.A., Yang, K., Bil, B.W., Blake, K. L., Hyvärinen, T., 2011. Epidote–clinozoisite as a hyperspectral tool in exploration for Archean gold. Aust. J. Earth Sci. 58, 813–822.
Rodger, A., Laukamp, C., Haest, M., Cudahy, T., 2012. A simple quadratic method of absorption feature wavelength estimation in continuum removed spectra. Remote Sens. Environ. 118, 273–283.
Rowan, L.C., Schmidt, R.G., Mars, J.C., 2006. Distribution of hydrothermally altered rocks in the Reko Diq, Pakistan mineralized area based on spectral analysis of ASTER data. Remote Sens. Environ. 104, 74–87.
Sabins, F.F., 1999. Remote sensing for mineral exploration. Ore Geol. Rev. 14, 157–183.
Schmidt, R.G., 1976. Exploration for porphyry copper deposits in Pakistan using digital processing of Landsat-1 data. J. Res. U.S Geol. Surv. 4, 27–34.
Seedorff, E., Dilles, J.H., Proffett Jr., J.M., Einaudi, M.T., Zurcher, L., Stavast, W.J.A., Johnson, D.A., Barton, M.D., Hedenquist, J.W., Thompson, J.F.H., Goldfarb, R.J., Richards, J.P., 2005. Porphyry Deposits: Characteristics and Origin of Hypogene Features. In: One Hundredth Anniversary Volume. Society of Economic Geologists (p. 0).
Sillitoe, R.H., 2010. Porphyry copper systems. Econ. Geol. 105, 3–41.
Singer, D.A., 2017. Future copper resources. Ore Geol. Rev. 86, 271–279.
Storch, T., Honold, H.-P., Chabrillat, S., Habermeyer, M., Tucker, P., Brell, M., Ohndorf, A., Wirth, K., Betz, M., Kuchler, M., Mühle, H., Carmona, E., Baur, S., Mücke, M., Löw, S., Schulze, D., Zimmermann, S., Lenzen, C., Wiesner, S., Aida, S., Kahle, R., Willburger, P., Hartung, S., Dietrich, D., Plesia, N., Tegler, M., Schork, K., Alonso, K., Marshall, D., Gerasch, B., Schwind, P., Pato, M., Schneider, M., de los Reyes, R., Langheinrich, M., Wenzel, J., Bachmann, M., Holzwarth, S., Pinnel, N., Guanter, L., Segl, K., Scheffler, D., Foerster, S., Bohn, N., Bracher, A., Soppa, M.A., Gascon, F., Green, R., Kokaly, R., Moreno, J., Ong, C., Sornig, M., Wernitz, R., Bagschik, K., Reintsema, D., La Porta, L., Schickling, A., Fischer, S., 2023. The EnMAP imaging spectroscopy mission towards operations. Remote Sens. Environ. 294, 113632.
Swayze, G.A., Clark, R.N., Goetz, A.F.H., Livo, K.E., Breit, G.N., Kruse, F.A., Sutley, S.J., Snee, L.W., Lowers, H.A., Post, J.L., Stoffregen, R.E., Ashley, R.P., 2014. Mapping advanced argillic alteration at cuprite, Nevada, using imaging spectroscopy. Econ. Geol. 109, 1179–1221.
Ürcher, L., Bookstrom, A.A., Hammarstrom, J.M., Mars, J.C., Ludington, S., Zientek, M. L., Dunlap, P., Wallis, J.C., Drew, L.J., Sutphin, D.M., Berger, B.R., Herrington, R.J., Billa, M., Kuşcu, I., Moon, C.J., Richards, J.P., 2015. Porphyry copper assessment of the Tethys region of western and southern Asia. In: U.S. Geological Survey Scientific Investigations Report 2010–5090–V: USGS.
Uribe-Mogollon, C., Maher, K., 2018. White Mica geochemistry of the copper cliff porphyry cu deposit: insights from a vectoring tool applied to exploration. Econ. Geol. 113, 1269–1295.
Uribe-Mogollon, C., Maher, K., 2020. White Mica geochemistry: discriminating between barren and mineralized porphyry systems. Econ. Geol. 115, 325–354.
van der Meer, F.D., van der Werff, H.M.A., van Ruitenbeek, F.J.A., Hecker, C.A., Bakker, W.H., Noomen, M.F., van der Meijde, M., Carranza, E.J.M., Smeth, J.B.D.,

Woldai, T., 2012. Multi- and hyperspectral geologic remote sensing: A review. Int. J. Appl. Earth Obs. Geoinf. 14, 112–128.
Van der Werff, H., Van der Meer, F., 2015. Sentinel-2 for mapping Iron absorption feature parameters. Remote Sens. 7, 12635–12653.
van Ruitenbeek, F.J.A., Cudahy, T.J., van der Meer, F.D., Hale, M., 2012. Characterization of the hydrothermal systems associated with Archean VMS-mineralization at panorama, Western Australia, using hyperspectral, geochemical and geothermometric data. Ore Geol. Rev. 45, 33–46.
Wallace, C.J., Maher, K.C., 2019. Phyllic alteration and the implications of fluid composition at the copper flat hydrothermal system, New Mexico, USA. Ore Geol. Rev. 104, 273–293.
Zhou, X., Jara, C., Bardoux, M., Plasencia, C., 2017. Multi-scale integrated application of spectral geology and remote sensing for green field gold exploration. In: Tschirhart, V.T., M. D (Eds.), Proceedings of Exploration '17: Sixth Decennial Interational Conference on Mineral Exploration – Integrating the Geosciences, pp. 899–910. Toronto.
Zürcher, L., Bookstrom, A.A., Hammarstrom, J.M., Mars, J.C., Ludington, S.D., Zientek, M.L., Dunlap, P., Wallis, J.C., 2019. Tectono-magmatic evolution of porphyry belts in the central Tethys region of Turkey, the Caucasus, Iran, western Pakistan, and southern Afghanistan. Ore Geol. Rev. 111, 102849.